TRACKING MACROPHAGES WITH ULTRASOUND

A Dissertation
Presented to
The Academic Faculty

by

Ashley Lenilla Alva

In Partial Fulfillment
of the Requirements for the Degree
Doctor of Philosophy in the
School of Electrical and Computer Engineering

Georgia Institute of Technology
December 2023

TRACKING MACROPHAGES WITH ULTRASOUND

Approved by:

Dr. Costas Arvanitis , Advisor
School of Mechanical Engineering
Georgia Institute of Technology

Dr. Stanislav Emelianov
School of Electrical and Computer Engineering
Georgia Institute of Technology

Dr. Levent Degertekin
School of Electrical and Computer Engineering
Georgia Institute of Technology

Dr. Brooks Lindsey
School of Electrical and Computer Engineering
Georgia Institute of Technology

Dr. Edward Botchwey
School of Bioengineering
Georgia Institute of Technology

Dr. Shu Jia
School of Biomedical Engineering
Georgia Institute of Technology

Date Approved: August 8th , 2023

Dedicated to my extraordinary parents,

Veronica and Santhan Alva

ACKNOWLEDGEMENTS

I want to start by thanking my advisor, Costas Arvanitis. I would not be here at this moment writing this acknowledgement for this thesis without him. I was fortunate that he took a chance on me many years ago. From the design of experiments to the rigorous interpretation of data, he has helped me understand the fundamental tenets of science. I was even more fortunate that he allowed me to work on this topic. This topic, many times, was my anchor when PhD got tough, and my experiments failed. Thank you, Dr Costas for your time, guidance and above everything, your patience with me.

I want to thank my committee members Dr Stanislav Emelianov, Dr Levent Degertekin, Dr Brooks Lindsey, Dr Shu Jia and Dr Edward Botchwey. Your time, intellectual contributions and insights have been invaluable throughout this process.

I would also like to extend my sincere thanks to the ECE Graduate office staff – Dr. Daniela, Tasha, and Dr. Klein. Your support from the very beginning has been instrumental in navigating the ins and outs of my graduate studies. Your assistance made my journey smoother and more manageable.

I'd like to extend my sincere gratitude to my lab mates- Scott, Yutong, Chulyong, Henry, Pradosh, Victor, Angie, Pranav, Shwetha, and Samhita, for their invaluable support and assistance throughout this journey. A few individuals warrant particular acknowledgement. Dr. Scott and Dr. Yutong deserve my special thanks for guiding me through many lab processes when I first started, their patience and expertise set a firm foundation for my work. Chulyong's pivotal contributions to the *in vivo* experiments featured in this thesis were indispensable and deserve special mention. Pradosh, a fantastic desk mate, was always there to lend an ear, sharing both my hardships and successes. Our daily interactions in the last year enriched my experience in many ways. Lastly, Pranav, my remarkable mentee, from whom I learned as much as I taught, if not more. Your curiosity and dedication kept me on my toes and pushed me to be a better mentor.

To all my wonderful friends from my many walks of life. Again, naming a few that have selflessly loved me, checked on me and taken care of me- Grad school (Kirti, Dr. Pratik, Dr. Aditi, Dr. Aline, Dr. Jimmy, Dr. Dhruv, Akshay, Ajit, Shalaka, Dr. Srinivas, Nivedita, Dr. Yusuf, Dr. Duygu, Sait, Dr. Faaiz, Dr. Tarun, Dr. Roopali), undergrad (Achu, Disha, Bella), school (Karina, Dr. Shwetha, Gemma, Aishu, Ann, Alka). A special thanks to Aline and Kirti, who reintroduced me to my faith during this critical phase. The depth of your faith and spirituality has been a profound inspiration, and I consider myself fortunate to have been a witness to it.

To my in-laws, Sujatha, Dr Surappa, Suchi, Paapu and Vinay, your support and encouragement have been invaluable. Your faith in me and my work has been a driving force, and for that, I am eternally grateful. Thank you for embracing me as part of your family, and for your constant encouragement and love.

Words fall short when I think of expressing my gratitude to Sohan and Rewis. Sohan, you ignited my PhD aspirations in 5th grade. Your unwavering support has been my stronghold - from your vigilance on r/Gatech, ensuring I was on top of every update, to teaching me how to code or to being my most enthusiastic cheerleader when I needed encouragement. Having you as a brother has been one of my greatest blessings, and you will forever remain a beacon of inspiration and a role model in my life. Rewis, my wonderful sister-in-law, your selflessness knows no bounds. When homesickness struck, you flew to Atlanta without hesitation, providing the comfort and support I needed. You played a crucial role in this journey, and I can't thank you enough for that.

To my mom, Veronica Alva and Dad, Santhan Alva who are my twin pillars without whom I cannot stand. Your unwavering faith in my potential allowed me to dream without boundaries and pursue who I wanted to be. You filled my life, from childhood (to adulthood), with unending encouragement, love, laughter, adventures, and countless books that profoundly shaped me and my dreams. Your tireless dedication and determination in your own work served as my inspiration and exemplified the true value of hard work. Thank you for everything.

Lastly, my sincerest thanks go to my husband and best friend, Dr. Sushruta Surappa, an exceptional scientist, and role model. Meeting you at Georgia Tech was indeed one of the best things that happened to me. Despite the physical distance that currently separates us, your love and companionship from across the coast never made me feel alone. You patiently listened to my thesis ramblings and let me practice my talks, showing unwavering interest and support. For all this and so much more, thank you.

TABLE OF CONTENTS

LIST OF TABLES

LIST OF FIGURES

LIST OF SYMBOLS AND ABBREVIATIONS

AM	Amplitude Modulation
AMPI	Amplitude Modulation Pulse Inversion
B-Mode	Brightness Mode US
CT	Computerized Tomography
CBNR	Contrast to background noise ratio
dB	decibels
DI	Deionized
DMEM	Dulbecco's Modified Eagle Medium
Hz	Hertz
m	meter
ml	milliliter
MB	Microbubbles
MΦ	Macrophages
MB-MΦ	MB labeled Macrophages
MHz	Megahertz
MRI	Magnetic Resonance Imaging
MI	Mechanical Index
OI	Optical Imaging
Pa	Pascals
PET	Positron Emission Tomography
PI	Pulse Inversion

PNP	Peak negative Pressure
ROI	Region of Interest
SNR	Signal to noise ratio
US	Ultrasound
µl	microliter

SUMMARY

Imaging macrophage trafficking can reveal important molecular, cellular, and functional characteristics of the host tissue and support the discovery of new biomarkers for improved diagnosis, prognosis, and treatment monitoring. Over the past years, macrophage imaging using different modalities has undergone significant development, however existing modalities offer suboptimal tradeoffs between depth of penetration, specificity, sensitivity, and resolution. Although ultrasound could potentially address this challenge, while also providing portable assessment (e.g., in an outpatient setting) at potentially lower costs, there is a paucity of investigations using ultrasound for macrophage imaging. The central hypothesis of this thesis is that labelling macrophages with microbubble contrast agents to augment their contrast, can enable imaging of macrophage trafficking with high sensitivity deep into tissues without compromising resolution. In this study, we showed that macrophages can be effectively labeled with microbubbles, identified ultrasound exposure settings where they can retain high echogenicity and viability without affecting their migratory capability and confirmed that they can produce a strong image contrast *in vivo* for an extended period of time. Finally, we were able to demonstrate that we can monitor the trafficking of intravenously administered microbubble labeled macrophages in breast tumor-bearing mice. This research, thus, provides a novel framework for macrophage imaging and tracking using ultrasound to support the discovery and clinical translation of new ultrasound methods and technology for macrophage-based diagnostics and therapy monitoring.

CHAPTER 1. INTRODUCTION

Macrophages are important immune cells that maintain tissue homeostasis by engulfing and digesting pathogens, cellular debris, and other foreign substances through a process called phagocytosis [1]. It has been shown that macrophages not only have the highest capacity to phagocytose but also a very high variability when it comes to phagocytosing [2]. They also serve as antigen presenting cells where they break down the antigens in phagocytosed pathogens and present them on their surface using major histocompatibility complex (MHC) molecules. They are also capable of regulating immune response by being involved in the production of various cytokines which are small signaling molecules. In response to infections or inflammation due to injuries, they can secrete pro inflammatory cytokines such as interleukin-1 (IL-1), interleukin-6 (IL-6), and tumor necrosis factor-alpha (TNF-alpha)[3]. They can also prevent excessive inflammation and tissue damage by releasing anti-inflammatory cytokines like interleukin-10 (IL-10) and transforming growth factor-beta (TGF-beta), which help dampen the immune response and promote resolution of inflammation[4]. Macrophages also help remove dead cells and debris from damaged tissue and they can promote tissue regeneration by releasing growth factors [5]. Macrophages are thus involved in an indispensable capacity in various diseases by performing these functions [6]. In particular to cancer, macrophages play a very critical role. Macrophages have a strong attraction to tumor based inflammation and can respond to the tumor's chemotactic cues, cross biological barriers, penetrate, and accumulate in the tumor[7]. This attraction can be so strong, that sometimes up to 50% of a tumor microenvironment can be composed of macrophages [8]–[10]. This accumulation and

distribution to the host tissue is increasingly considered as a robust prognostic marker for cancer [11]. In addition to their increasing role in diagnosis and prognosis of human disease, chimeric antigen receptor macrophages are currently in trials for cancer immunotherapy [12]. These investigations not only demonstrate their capacity for therapy, but also emphasize the need for methods to track their trafficking to facilitate their effective translation to the clinic (e.g., identify non-responders, assess off target toxicity etc.) [13], [14]. Therefore, noninvasive strategies for tracking macrophage trafficking could provide critical prognostic and diagnostic information as well as guide macrophage based therapeutic interventions against a range of deadly diseases, including cancer.

1.1 Tracking Macrophages

To track immune cells including macrophages in vivo, it is required that these cells are labeled. We will be discussing the cells that are "directly labeled" only as this method does not involve genetic modification and hence is easily transferable to clinical practice due to less regulatory scrutiny. In principle, direct cell labeling requires that the cells are labeled by some natural process like phagocytosis or pinocytosis, direct attachment to the cell membrane or uptake through some transporter expressed on cell surface. This process is usually done *ex vivo*. Once modified, these cells are administered into the subject and the subject is imaged to enable cell detection *in vivo*.

With imaging, there have been many attempts to track macrophages and other immune cells using MRI, CT, PET amongst others summarized in table 1. However, none have emerged as a front runner due to some inherent shortcomings in depth of penetration, specificity, sensitivity, and resolution. MRI has been widely used for tracking cells

particularly with magnetite (Fe_2O_3)-based superparamagnetic iron oxide nanoparticles (SPIONs). However, while this method is sensitive (10^6 cells per ml) and has whole body imaging capability, it does lack specificity [15]. Fluorine-19 (^{19}F) MRI addresses the specificity issue with iron based cell tracking as endogenous ^{19}F is low *in vivo* but suffers in terms of sensitivity [16], [17] . PET provides whole body imaging capability and excellent sensitivity down to detecting 1 cell but is limited in terms of spatial resolution and requires very dedicated systems that are not yet clinically translatable [18]–[20]. On the other hand while optical imaging and (micro) CT have had successful preclinical trials, they face several challenges in scaling up [21]–[23]. Optical imaging provides single cell resolution but has limited depth penetration. CT has whole body imaging capability but has low sensitivity and requires high doses of radiopaque agents to accumulate. Thus, complementary cell tracking methods are needed to support the discovery and clinical translation of macrophage-based diagnostics and therapeutic interventions. High sensitivity, specificity, and penetration depth without compromising resolution while also providing portability and potentially lower costs are requirements for this imaging technology to be capable of tracking macrophages.

Table 1 : Comparison of imaging modalities for cell tracking

Imaging Modality	Cells tracked	Tracer	Resolution [mm]	Temporal resolution [mins]	Sensitivity (detection limit) [cells/ml]	Specificity	Portability [Y/N]	Field of view	Ref
PET	CAR-T cells	^{68}Ga-DOTATOC, [^{18}F]-TMP,	1.4	10	10^3	High	No	Whole body (WB)	[19], [20]
PET-CT	MDA-MBA-231	^{68}Ga-MSN	`1.7	10	1	High	No	WB	[18]
MRI (3T)	Dendritic cells	SPION, Fluorine-19 [^{19}F]	0.5	~10	10^3 w/ SPION, 10^5 w/ ^{19}F	High w/ SPION, Low w/	No	WB	[15], [16], [24]
µCT	MSC	Gold-Poly-L-Lysine nano particles	0.25-1.5	0.2-10	$10^3 - 10^4$	High	No	WB	[25], [26]
Optical Imaging	MSC	DiD	0.02	0.01	~10	High	No	0.1 x 0.1	[27]–[29]
Photoacoustic Imaging	MSC	Gold Nano Rods-Si35,Gold nano spheres	0.1	1	~10^3	High	No	10 x 10	[30], [31]
US (7 MHz)	Neural	MB	0.2	0.001	1	High	Yes	10x10	[32]

1.2 Tracking Macrophages with US

Ultrasound (US) imaging can potentially satisfy several of the key requirements for tracking macrophage trafficking at clinical scales. Most notably, it is a mobile, non-ionizing, low-cost technology and is available worldwide easing translation. Additionally, US has really high temporal resolution i.e. real time imaging capabilities and at high frequencies, high spatial resolution.

The basic approach in US is based on radar like pulse echo methods. The process begins with a handheld device called transducer that consists of a probe that can convert electrical energy and emit sound wave or receive sound waves and convert them back to electrical energy. In US, these sound waves are typically between 1-10 MHz in the clinic depending on the application[33]. Pulses of US are directed into the body and allowed to interact with body structures. A fraction of the US energy is scattered or reflected to the transducer. Reflection happens when the sound waves encounter a boundary between two tissues with different acoustic properties like density and speed of sound (also known as acoustic impedance). The amount of reflection depends on the difference in acoustic impedance between the two tissues. Scattering, on the other hand, occurs when two conditions are met- 1) a sound wave strikes a structure with a different acoustic impedance to the surrounding tissue and 2) sound wave strikes a structure which is smaller than the wavelength of the incident sound wave. In clinical ultrasound imaging, both reflection and scattering contribute to the formation of the image.

Reflected sound waves carry information about the tissue boundaries and interfaces, while scattered sound waves contribute to the overall texture and detail of the

image. By analyzing the reflected and scattered waves, the ultrasound system can reconstruct an image that represents the internal structures of the body. Since macrophages are much smaller (~20μm) than the wavelength we use clinically or for research purposes, we will focus on scattering. Scattering cross section (σ_S), a metric of scattering, can be thought of as the area of the incident wavefront on the scatterer that contains an amount of incident power equal to the scattered power (P_s). Mathematically, from the Rayleigh model, it can be shown that σ_s and P_s for small scatterers are given by equation 1 and equation 2 respectively [34], [35],

$$\sigma_s = 4\pi\alpha^2(k\alpha)^4)\left[\left(\frac{K_0 - K_S}{3K_0}\right)^2 + \frac{1}{3}\left(\frac{\rho_S - \rho_0}{2\rho_S + \rho_0}\right)^2\right], k\alpha \ll 1 \quad (1)$$

$$P_s = -P_i\frac{e^{-ikr}k^2\alpha^3}{r}\left\{\frac{K_0 - K_S}{3K_0} + \frac{(\rho_s - \rho_0)}{2\rho_s + \rho_0}\cos\theta\right\} \quad (2)$$

Where α is radius of scattering element, k is wave number, K_0 and K_s are the bulk modulus of medium and scattering element respectively, ρ_0 and ρ_s are the mass density of medium and scattering element respectively, r is radius of scattering element and $\theta$is axis of propagation. The goal in any imaging is to have a high signal to noise ratio which is related to high amplitude of echoes returning to the transducer or high scattering. Notice that there are multiple ways to increase the σ_s in equation 1 . The first is increasing frequency up to the clinical requirement of 10 MHz as $\sigma_s \propto f^4$. Secondly, increasing the

size of scatterer as $\sigma_s \propto \alpha^6$ but there is a clinical upper limit of 10 μm so scatterers can enter capillaries [36]. Changing the density of the scatterer could also potentially increase the σ_s but it cannot exceed 1/3 $\left(\lim_{\rho_S \to 0} \frac{1}{3}\left(\frac{\rho_S - \rho_0}{2\rho_S + \rho_0}\right)^2 = \frac{1}{12}\ ,\ \lim_{\rho_S \to \infty} \frac{1}{3}\left(\frac{\rho_S - \rho_0}{2\rho_S + \rho_0}\right)^2 = \frac{1}{3}\right)$. Placing similar limits on compressibility shows that, in theory, differences in compressibility of the scatterer can have enormous impact on σ_s, as its magnitude can change by several orders for realistic materials. $\left(\lim_{K_S \to 0} \left(\frac{K_0 - K_S}{3K_0}\right)^2 = \frac{1}{9}\ ,\ \lim_{K_S \to \infty} \left(\frac{K_0 - K_S}{3K_0}\right)^2 = \infty\right)$. It was demonstrated that the σ_s of an air bubble of 1 μm is 100 million times more than that of a rigid iron sphere of the same size [37] .

While macrophages and surrounding cells like cancer cells are not as rigid as iron spheres, they are not as compressible as gas either leading to negligible contributions to σ_s and hence, essentially identical σ_s and low imaging contrast (scattered power) as seen in Table 2. The realization that compressibility of gas can go up to $\sim 1 \times 10^{-7}$ Pa^{-1} compared to tissue and plasma which are around $\sim 1 \times 10^{-10}$ Pa^{-1} led to the development of microbubble Ultrasound Contrast Agents (USCA) [38]. **In this thesis, we hence hypothesize that in order to visualize macrophages and differentiate them from surrounding cells using US imaging, we will need to label the macrophage with microbubbles (MBs) to augment their scattering cross section and enable detection and tracking of macrophages at high sensitivity deep in the tissue without sacrificing resolution.**

However, It is crucial to consider the resonance effect when using MBs as a contrast agent. This resonance occurs because enclosed volume of gas acts like a spring and mass of the liquid around the bubble acts as inertia. For an unencapsulated gas bubble in an

isotropic medium, the resonant frequency is given by Equation 3. This resonant frequency depends on parameters such as the ratio of specific heat capacity at constant pressure and volume (γ), total pressure (P_H) which includes incident pressure P_I and density of the surrounding medium (ρ_0) [39], [40]. Hence the modified σ_{sR} and P_{sR} are given by equation 4 and 5 where the R subscript denotes resonance. It should be noted that σ_s does not include damping or non-linearities. By referring to Table 2, one can observe that the scattered power of MBs is five orders of magnitude greater than that of a macrophage and cancer cell.

$$f_r = \frac{1}{2\pi\alpha}\sqrt{\frac{3\gamma P_H}{\rho_0}} \tag{3}$$

$$\sigma_{sR} = 4\pi\alpha^2\left[\frac{1}{\left(f_r^2/f^2 - 1\right)^2 + \left(f_r^4/f^4\right)(k\alpha)^2}\right] \tag{4}$$

$$P_{sR} = \frac{1}{P_I}\left[\frac{1}{\left(f_r^2/f^2 - 1\right)^2 + \left(f_r^4/f^4\right)(k\alpha)^2}\right]^{1/2} \tag{5}$$

Table 2 : Scattering cross section and scattered powder for different elements

Scatterer	Size $[\mu m]$	Density $\boldsymbol{\rho_S}$ $\left[\frac{kg}{m^3}\right]$	Speed of sound **C** $\left[\frac{m}{s}\right]$	Compressibility $\boldsymbol{K_S}$ $[Pa^{-1}]$	Polytropic Exponent $\boldsymbol{\gamma}$ $[unitless]$	Resonant frequency $\boldsymbol{f_R}$ `$[MHz]$	Scattering cross section ** $\boldsymbol{\sigma_s}$ $[\mu m^2]$	Scattered Power *** $\boldsymbol{P_s}$ $[\mu W]$	Ref
Macrophage	20	1097	1489	4.1e-10	7.15*	0.17	18.15e-5	1.4e-11	[41]
Cancer cell	20	1068	1489	4.2e-10	7.15*	0.17	8.98e-5	0.7e-11	[42], [43]
MB	1-3	1.21	1540	3.5e-7	1.14	1.35	87.685	7.1e-6	[44] – [46]

* Polytropic exponent for cytoplasm used

** All values calculated with clinical frequency of **3 MHz**

***Incident power assumed to 500 Kpa which lies within the typical acoustic pressure levels *in vivo*[47]

It can be seen from equation 3 that the resonant frequency, f_r is inversely proportional to the radius. Although this equation and subsequent equations 4 and 5 provide a simplified representation and does not consider factors like surface tension (which can increase the resonant frequency) or viscous losses (which can decrease it), it does indicate that operating at the resonant frequency would result in an increase in σ_s .

In Table 3 , in this idealized condition, operating at resonance frequency gives scattering cross section and scattered power 6 orders of magnitude higher. However, Table 3 also indicates that even at non-resonant frequencies between 3-18 MHz, we are still able to obtain sufficient scattering cross section and consequently sufficient scattered power to distinguish a MB from a macrophage and other surrounding cells.

Considering these findings, it's worth noting that we utilized a L22-14v transducer (Vermon) operating in the range of 14-22 MHz, with a center frequency of 18 MHz. Given that our research was carried out using a mouse model, using these higher frequencies was feasible and allowed for higher resolution. More specifically, we utilized frequencies of 15.625 MHz and 18 MHz and this data supports the rationale that we can obtain adequate scattering even at higher frequencies.

Table 3 : Effects of resonance on scattering cross section and scattered power

Frequency f $[MHz]$	Usage	Scattering cross section $\boldsymbol{\sigma_s}$ $[\mu m^2]$	Scattered Power $\boldsymbol{P_s}$ $[\mu W]$
1.9	Resonant frequency	~4.3e7	~3.5
3	Clinical frequency	87.685	7.1e-6
15.625	Research frequency 1	29.79	2.4e-6
18	Research Frequency 2	29.76	2.4e-6

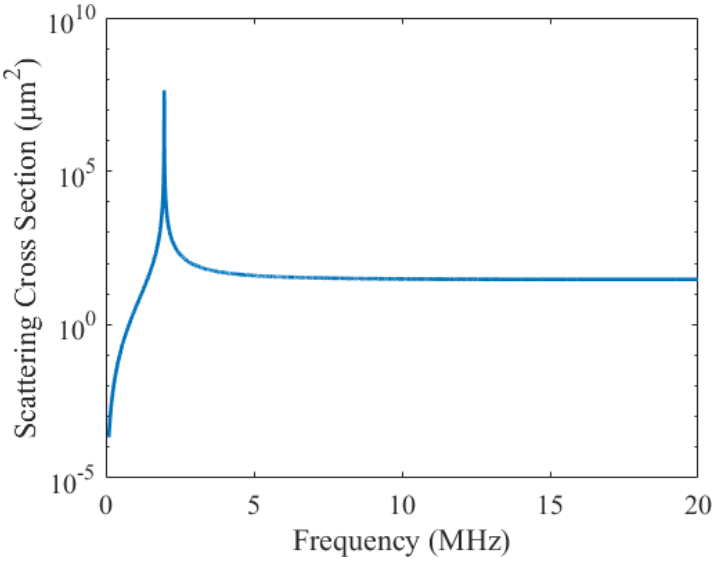

Figure 1: Scattering cross section vs frequency for a MB

CHAPTER 2. ENGINEERING AND CHARACTERIZING MB LABELED MACROPHAGES

2.1 Labeling macrophages with MBs

As a first step, we developed a protocol to label macrophages with MBs through incubation. This approach was chosen based on the well-known capability of macrophages to phagocytose a wide variety of particles [2]. Investigations in the past have also shown the macrophages can also phagocytose MBs [48], while retaining their functionality *in vivo* [49].

Macrophages need to be labeled with MBs *ex vivo* while adhered to the well plate, and the reasons for this are multifold. Firstly, phagocytosis is a time dependent process depending on particle size and shape [50] [51], [52] and requires the contact of MBs to the macrophages. By fixing the macrophages without fluid flow, such as blood, it allows for a longer duration of contact, thereby increasing the efficiency of phagocytosis. Moreover, the kinetics of microbubbles is relatively fast (less than 5 minutes), which can be much shorter than the duration required for phagocytosis (ranging from approximately 6 to 360 minutes) [48], [51].Secondly, labeling macrophages *ex vivo* with only macrophages and microbubbles present offers a specificity advantage. While various cells *in vivo* have the potential to perform phagocytosis, macrophages exhibit a significantly higher magnitude of phagocytic activity compared to other cell types [53]. Consequently, by conducting the labeling process *ex vivo*, it becomes possible to track and monitor exclusively those

macrophages that have been labeled, enabling precise identification and analysis. However, it is worth noting that this specificity concern could potentially be addressed by employing targeted microbubbles designed specifically for macrophages [54], [55]. Lastly, and more importantly, MBs, due to their micron size, cannot extravasate vasculature [56], [57].

In our investigations, we used mouse RAW264.7 macrophages. This cell line is a macrophage-like cell line originating from Abelson murine leukemia virus and derived from BALB/c mice and is frequently used for testing new immune cell imaging methods [58]. Throughout our studies, we ensured passage numbers were below 30 as surpassing this threshold could influence data reliability [58].

We started with Definity MBs, a clinically approved US contrast agent indicating biocompatibility and a good safety profile. Definity has a lipid shell and Octafluoropropane gas (C_3F_8), a gas which is highly compressible. This high compressibility leads to strong scattering of microbubbles which is essential for producing high contrast in US images. In addition, they are also sized between 1.1 to 3.3 μm. This size allows them to be taken up by macrophages, which have been shown to phagocytose particles in this size range [59]. Definity also has higher stability compared to other contrast agents which may allow for sufficient time for interaction with macrophages and subsequent labeling [60].

2.1.1 The assay

We first plated the macrophages in a 96 well plate and allowed them to adhere overnight. The next day we added Definity MBs diluted in cell culture media. For media, we used Dulbecco's Modified Eagle Medium or DMEM which was supplemented with 10% fetal bovine serum (FBS) and 1% penicillin/streptomycin to the adhered macrophages

(Figure 2a). Now due to buoyancy, the MBs will float to the top. To get MBs in contact with the adhered macrophages, we inverted the dish. Prior to inversion, we also filled the well with media to ensure no air pockets that could form during the inversion. We then used parafilm to seal the plate, as it permits gas exchange while being resistant to moisture, thus preventing leakage. The sealed plate was incubated at 37°C in a humidified environment containing 5% CO2 for four distinct time intervals. Parafilm was chosen as a sealant because it is gas permeable but moisture resistant hence no leakages. Following incubation, the plate was reverted to its original upright position, and excess media were eliminated. This step also removed non-adherent macrophages (which are non-viable) and any MBs that did not adhere. Lastly, we washed the cells three times using media and proceeded with imaging .

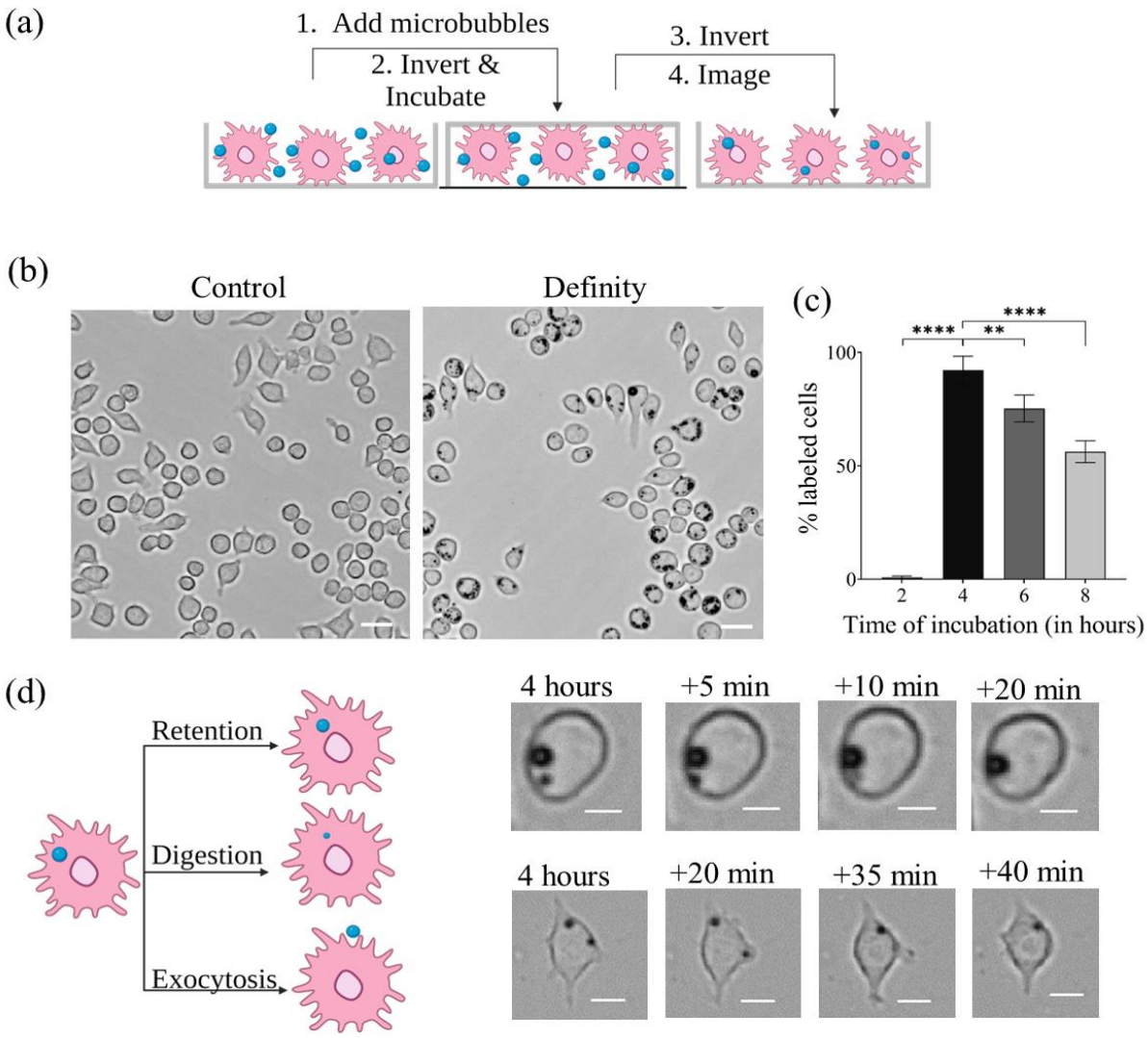

Figure 2: More than 90% of RAW264.7 macrophages can be labelled with Definity microbubbles via phagocytosis

(a) Experimental setup to label RAW264.7 macrophages (MΦ) with microbubbles (MB). (b) Representative images of MΦ incubated with and without MBs (black dots) showing more than 90% (92% ± 6%) of the RAW264.7 MΦ have been labeled successfully following 4 hours of co-incubation with Definity MBs. Scale bar 20 µm. (c) Quantification of the MB-labeling persistence, demonstrating that 50% (56.26% ± 4.8%) of MΦ remain labeled for at least 8 hours. (d) fate of the MB withing MB-MΦ follows three possible routes- retention (which is most favorable for us) and processes resembling MB digestion and exocytosis

On imaging, we found that 4 hours incubation produced robust labeling of the RAW264.7 macrophages (92.25% ± 6.08% of macrophages, n=4, p-value<0.0001; Figure 2 b-c) henceforth referred to as MB-MΦ. Moreover, we observed that the ingested MBs remain within the MΦs for several hours, where more than 56.26% (± 4.8%, n=4) of MΦ retained their MB for at least 8 hours. Interestingly, our microscopy data also showed that the MB-MΦ lose their MB post 4 hours in processes resembling MB digestion and exocytosis. In an *in vivo* environment, the release of MBs from MB-MΦ and their subsequent circulation is not an issue as Definity microbubbles are FDA-approved contrast agents and have been deemed safe for clinical use. The gas contained within the Definity microbubbles, octafluoropropane, is expelled through the respiratory system, while the lipid shell undergoes metabolism like other lipids and is ultimately excreted [61]. It would be interesting, in future work, to optimize characteristics of the MB such as size and surface chemistry that may allow for prolonged retention if the application demands it [62]

2.2 Optimizing phagocytosis

We then aimed to optimize this assay based on phagocytosis to make it more efficient. Given that phagocytosis is influenced by attributes of the target, we sought to optimize 2 properties of the MB [51], [59]. Utilizing Definity as a reference, we experimented with different shell compositions - lipid shells, which are analogous to Definity, and mannosylated lipid shells. We chose mannosylated lipid shells because previous studies have demonstrated that mannose enhances the efficiency of phagocytosis [63]. Beyond bubble coating, stability or persistence of microbubble can also be very important. Firstly, in the case of lipid MBs, we saw that the best labeling occur at 4 hours

and hence the microbubbles would need to be stable for that duration [48], [50]. Under this stability hypothesis, we evaluated microbubbles with different gas cores (Octafluoropropane vs. Decafluorobutane) to examine their impact on microbubble persistence time. Mathematically, persistence time can be described by the Epstein Plesset equation (Equation 6,[64]).

$$\frac{d\alpha}{dt} = D_g L \left(\frac{\frac{C_i}{C_s} - 1 - \frac{2\sigma}{\alpha P_o}}{1 + \frac{4\sigma}{3\alpha P_o}} \right) \left[\frac{1}{\alpha} + \frac{1}{\sqrt{\pi T_p D_g}} \right], \tag{6}$$

$$T_p \propto \frac{\rho_g \alpha^2}{2 D_g C_S} \tag{7}$$

Where α is the radius of the microbubble, D_g is the diffusion coefficient of gas, L is gas solubility coefficient, C_i is dissolved gas concentration, C_s is saturation coefficient of gas, σ is the surface tension and P_0 is ambient pressure, T_p is the time for microbubble persistence and ρ_g is the density of core gas. If surface tension from the shell is neglected for both simplicity and the fact that the same shell and medium are used, Equation 7 [65] can be derived. Along with Table 4[66], it can be seen how Decafluorobutane might persist longer than Octafluoropropane. Specifically, the persistence time of Decafluorobutane is about 4.8 times longer than Octafluoropropane using equation 7 . Throughout this study, all MBs filled with Octafluoropropane are denoted with an 'O,' while those with Decafluorobutane are denoted with a 'D'.

Table 4: Persistence of different MB gas cores

Perfluorocarbon	Density ρ_g [x10^{-3}g /cm3]	Solubility C_s [x10^{-6}g/mL]	Diffusion coefficient of gas D_g [x10^{-6} cm^2/s]
Octafluoropropane	10.3	5.66	7.72
Decafluorobutane	11.2	1.44	6.86

We then proceeded to make the different MBs according to the protocol previously described in [67], [68]. The MB with a lipid only shell was prepared using a 9:1 molar ratio of 1,2-distearoyl-sn-glycero-3-phosphocholine (DSPC) and 1,2-distearoyl-sn-glycero-3-phosphoethanolamine-N-methoxy(polyethylene glycol)-2000 (DSPE-PEG2000) (Avanti Polar Lipids, Alabaster, AL, USA) in a solution containing propylene glycol 15% (v/v), glycerol 5% (v/v) and phosphate-buffered saline (PBS) 80% (v/v). After degassing of the lipid solution in 3-mL glass vials, the headspace of the vial was filled with either octafluoropropane gas or decafluorobutane gas. The MBs with a mannose/lipid shell was prepared using a 9:0.5:0.5 molar ratio of 1,2-distearoyl-sn-glycero-3-phosphocholine (DSPC), 1,2-distearoyl-sn-glycero-3-phosphoethanolamine-N-methoxy(polyethylene glycol)-2000 (DSPE-PEG2000) (Avanti Polar Lipids, Alabaster, AL, USA) and 1,2-distearoyl-sn-glycero-3-phosphoethanolamine-N-(polyethylene glycol)-Mannose

(Xi'an Ruixi Biotechnology, China) in a solution containing propylene glycol 15% (v/v), glycerol 5% (v/v) and phosphate-buffered saline (PBS) 80% (v/v). After degassing of the lipid solution in 3-mL glass vials, the headspace of the vial was filled with either octafluoropropane gas or decafluorobutane gas. MBs were formed by agitation using a Vialmix device (Lantheus Medical Imaging, North Billerica, MA, USA).

Our results indicated that MBs with the low diffusivity gas Decafluorobutane did in fact lead to higher uptake by RAW264.7 macrophages as compared to the higher diffusivity gas Octafluoropropane (Figure 3, b-c). Considering that lower gas diffusion from the bubble leads to more stable bubbles, our hypothesis suggesting that MB stability is a key MB property for effective MB uptake by macrophages seems plausible. The importance of MB stability is further supported by our observations using the significantly more stable and FDA-approved MB formulation, Definity, that demonstrated more efficient macrophage labeling as compared to our custom-built MBs, including mannose-based formulations. While additional work is necessary to clarify the role of the inner gas core and optimize the formulation ratios of mannose-based MBs, our data demonstrate that Definity is a good candidate for the remainder of the studies.

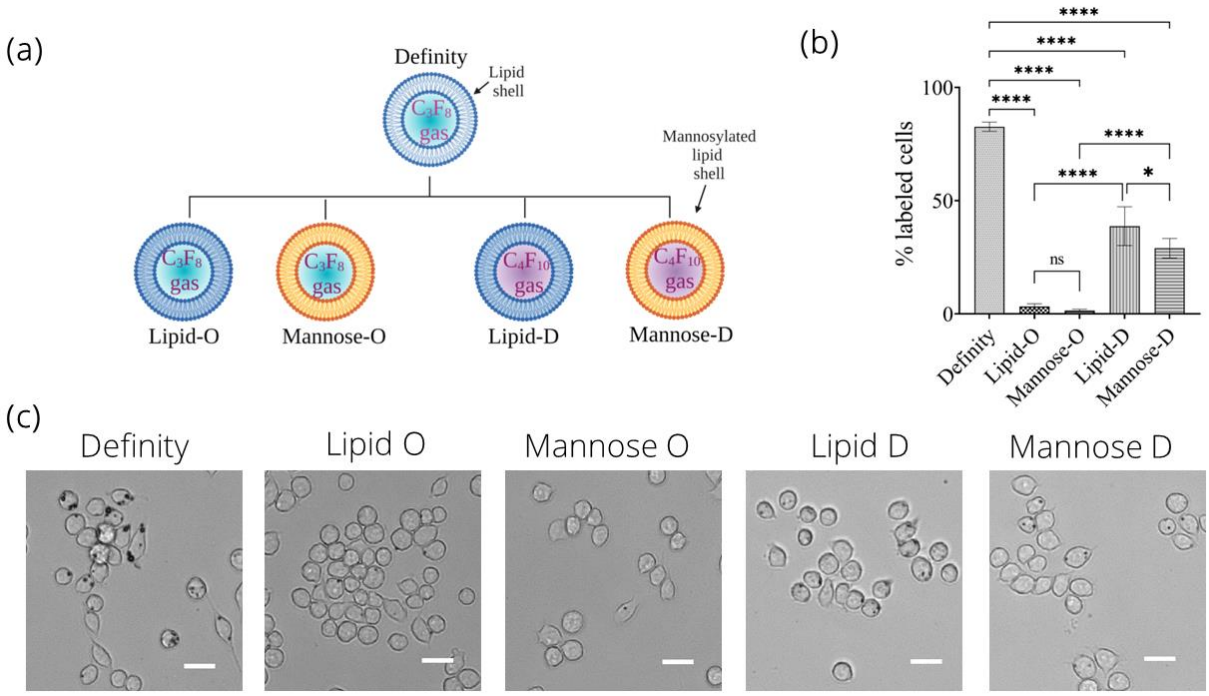

Figure 3 :Optimizing phagocytosis

a) Lipid microbubbles with different shell composition (mannose shell vs lipid shell) and gas core (Octafluoropropane – C_3F_8 – labeled with 'O' vs Decafluorobutane – C_4F_{10} – labeled with 'D') that were developed in house. By using, FDA approved microbubble Definity as a model, the properties of shell composition and gas core were chosen. b) Quantification of the labeling efficiency with the different bubble types c) Representative Images showing the labeling of the RAW264.7 macrophages with the different microbubbles on 4 hours of co-incubation. Scale bar 20 µm. P values were determined by one-way ANOVA followed by Tukey's multiple comparisons. ****P < 0.0001;n.s. - not significant.

2.3 Assess echogenicity and viability of MB-MΦ

As alluded to previously, when an US wave strikes a MB, it oscillates by expanding and contracting in response to pressure changes. Due to the compressible nature of the gas inside the MB and the elasticity of the shell, even a small change in pressure can cause a

relatively large change in the volume of the MB. Thus, MBs are nonlinear and can produce harmonics even at low pressures.

To assess their echogenicity, we sonicated MB-MΦ plated on a mylar film well plate from the bottom with a focused ultrasound transducer (FUS). Illustration of this setup is provided in Figure 4. The echoes were received by a passive cavitation detector (PCD), which was positioned coaxially within the hole of the FUS. The FUS transducer is driven at 0.5 MHz with 20 cycles and increasing MI generated by a function generator (Picoscope 5000D, Pico Technology) and further amplified by a 50-dB power amplifier (model 240L, Electronics & Innovation Ltd). The short number of cycles were chosen to prevent any potential detachment. On the receiver side, the PCD is connected to a high pass filter with a cut-off at 0.6 MHz to prevent saturation due to strong fundamental frequency signal. The signal is then fed to a data acquisition system (Picoscope 5000D, Pico Technology) and analyzed using fast Fourier transform from the host computer. In this study, the calibration was carried out in water (specifically in a free field setting) using a 2mm needle hydrophone from Precision Acoustics.

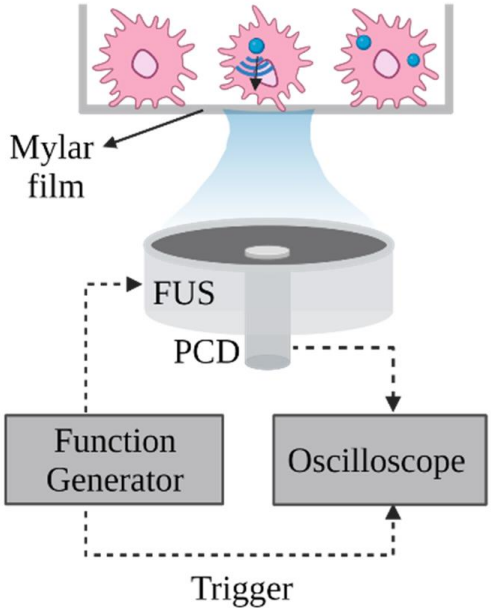

Figure 4 : Setup to assess echogenicity of MB-MΦ

We wanted to report all the pressures in MI as reporting just the peak negative pressure wouldn't provide a complete understanding of the potential for biological effects such as cavitation. This is because the likelihood of cavitation and possible mechanical damage depends not only on the pressure but also on the frequency of the US wave [69]. Moreover, regulatory bodies like the FDA have established limits on the Mechanical Index for medical US [70]. This standardization allows for a uniform way to assess and ensure safety universally [71]. The Mechanical index was computed using the equation 8 delineated below.

$$Mechanical\ Index = \frac{Peak\ Negative\ Pressure\ [MPa]}{\sqrt{Center\ frequency c}[MHz]} \quad (8)$$

Additionally, we assessed the viability of macrophages by imaging both MΦ (control) and MB-MΦ using the ReadyProbes® Cell Viability Imaging Kit (Life Technologies, Gaithersburg, MD, USA) before and after exposure to ultrasound waves. The kit contains a NucBlue Live reagent to stain all nuclei, while NucGreen Dead reagent was used exclusively for staining dead cells. The proportion of dead cells was determined by manually counting the number of dead cells and dividing it by the total number of nuclei. Our findings revealed that MΦ without MB labeling generated acoustic emissions exclusively at the fundamental frequency, even at the highest pressure tested (0.68 MI) (See Figure 5a, top panel). For these non-labeled macrophages, viability remained unchanged before and after exposure to ultrasound waves across all tested pressures (See Figure 5, top right).

Conversely, MB-MΦ were observed to emit harmonic components at all tested pressures (See Figure 5, bottom left). As the pressure was further increased, ultra-harmonics were also detected (See Figure 5, bottom left), and when the MI exceeded 0.34, there was an observed increase in broadband noise, which is indicative of an impulse response (i.e., microbubble collapse). Microscopy images also revealed a substantial increase in cell death ($n=4$, $p<0.0001$) at pressures where broadband noise was detected ($MI > 0.34$).

Taken together, our results show that microbubbles maintain their echogenic properties even after being labeled by macrophages. Additionally, our data suggests the

existence of an optimal ultrasound pressure window (0.08-0.34 MI) for imaging MB-MΦ, where maximum echogenicity is retained without significant alterations in cell viability

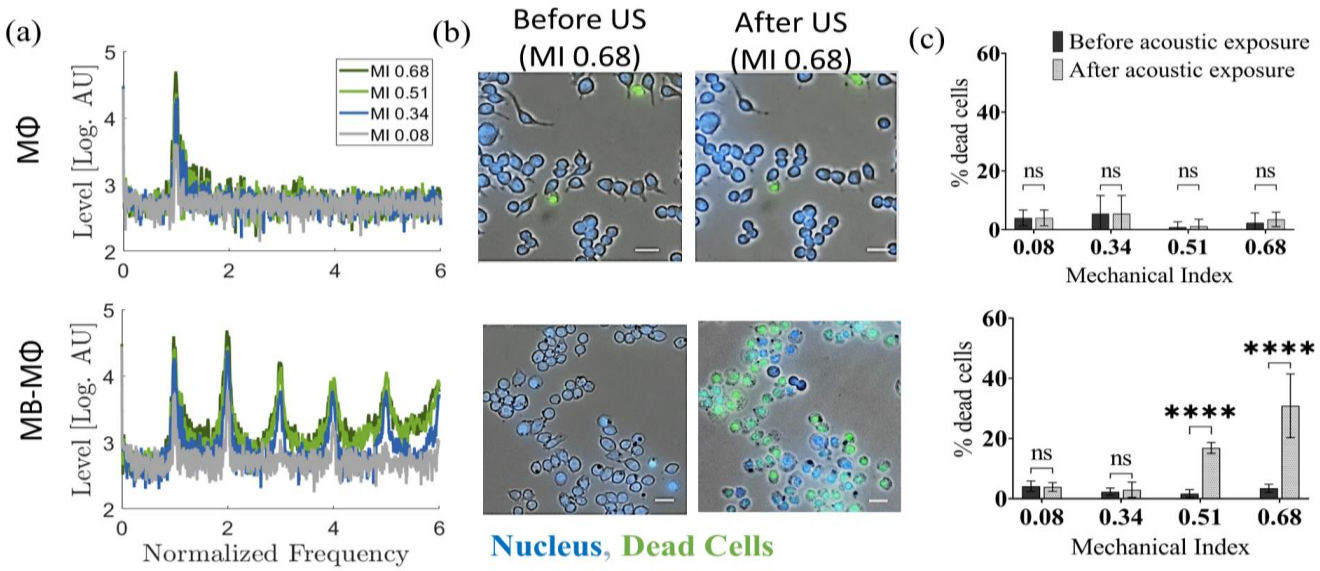

Figure 5: Sonicated MB-MΦ emit strong echoes within clinically relevant US exposure and retain high viability

(a) Impact of increasing MI on harmonic generation is assessed. In the top panel where MΦ are only present, even at the highest pressure, only the fundamental frequency is observed. In the bottom panel, in contrast to control, when MΦ are labeled with MBs, Harmonics are observed at all pressures and ultraharmonics as well as broadband start to manifest as the pressure is increased suggesting that labeling with MBs does indeed make the MΦ echogenic.(b) Representative microscopy images before and after acoustic excitation to show cell death at highest pressure in the case of MB-MΦ and no change in viability in the case of MΦ only. Green represents all the dead cells and blue represents all the nuclei (c) Impact of increasing MI on viability is assessed. In the case of MΦ only, viability is unchanged even at the highest pressure however in the case of MB-MΦ, viability is impacted negatively in the pressures where broadband occurs. This thereby establishes a window of operation (M1 < 0.34) where we see strong harmonics but no change in viability when tracking MB-MΦ

We have previously shown that the labeling efficiency is ~90% which implies there are some MΦ that are not labeled. Among the MΦ that seem to be labeled, there appears to be a significant reduction in their survival after being subjected to US. In contrast, the small number of MΦ that didn't appear to get labeled seemed to maintain their survival rate even after the US exposure. These observations are presented in Figure 6b. Although it is uncertain whether the labeling occurs through phagocytosis or via a different mechanism, the experiments suggest that the cell death of macrophages in response to inertial cavitation could be indicative of a robust attachment or potential phagocytosis.

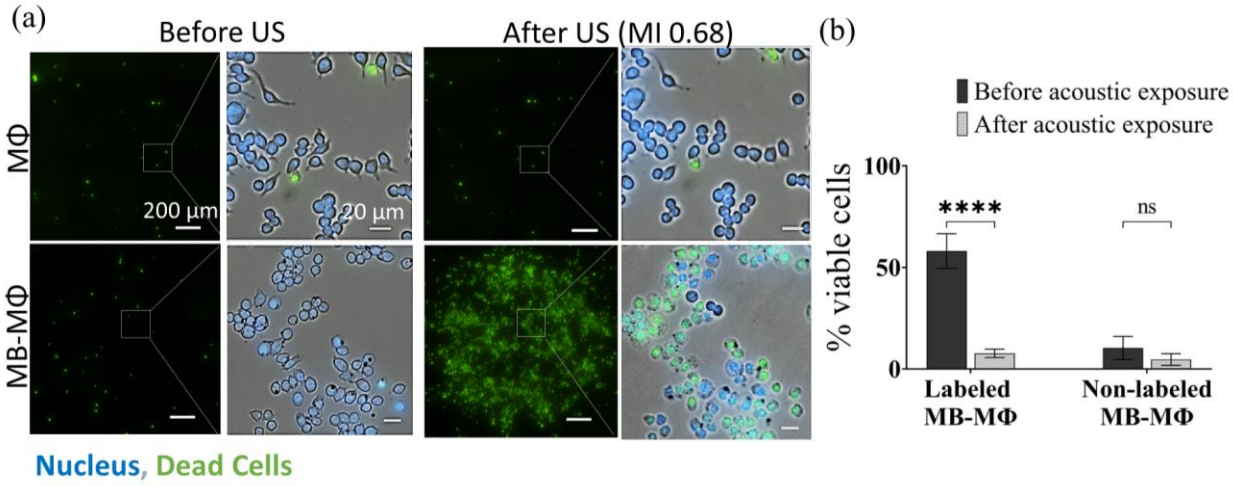

Figure 6 : MB-MΦ are firmly labeled (if not phagocytosed with MBs)

Microscopy images for MΦ and MB-MΦ before and after exposure to high acoustic excitation at peak negative pressure of (0.68 MI- beyond initial cavitation threshold). The representative images show cell death occurring in a radial pattern the size of the transducer focal size (2 mm). (b) Quantification of the lower right panel of 6a (after US, MB-MΦ). Not all MΦ get labeled even though they are incubated with MBs. This graph quantifies among the cells that were actually labeled, the viability significantly decreased after exposure to acoustic excitation. On the other hand, among the few MΦ cells that did not get labeled with microbubbles, their viability remained unchanged following the acoustic excitation. done using two way ANOVA for ****P < 0.0001 , n.s., not significant. (Prism 9; GraphPad).

2.4 Scaling up: Harvesting MB-MΦ

All the experiments presented till now had the cells adhered to a 96 well plate. If these MB-MΦ are to be used *in vivo* for imaging, they need to be harvested from the plates with both the cells and the labeled MB intact. To do so the protocol was modified as follows. The cells were plated in a larger dish - the Nunc™ EasYDish™ Dish (Thermofisher). This dish's design allowed for easy sealing via parafilm. Furthermore, the increased size of the dish not only facilitated scaling up the process but also allowed for the use of a cell scraper to detach cells. While trypsin is conventionally used to detach cells, it was shown to alter M2 surface markers and function[72]. After scraping, a gentle centrifugation step at 100 G for 20 seconds was included to further separate free bubbles from cells, with the low speed preventing pellet formation that could damage the MB-MΦ. This process is demonstrated in Figure 7 which shows the post-centrifugation results: the supernatant contains free MBs, while the precipitate primarily consists of MB-MΦ.

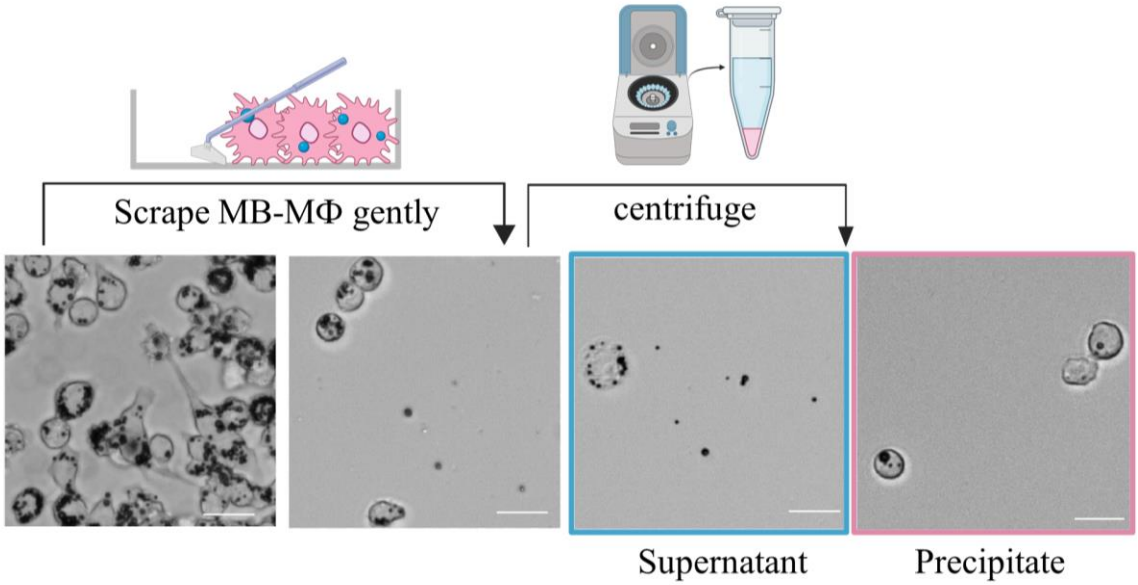

Figure 7 : Harvesting macrophages
MB-MΦ are plated according to previous protocol in a larger dish. Once washed, the MB-MΦ are scraped gently and centrifuged at low speed of 100 G for 20s. The supernatant which contains MB and dead MB-MΦ are discarded, and the precipitate is retained. Scale bar- 20 µm.

2.5 Assess migration capabilities of MB-MΦ

Macrophages' ability to migrate is critical for a robust immune response [73]. From their role, it is evident that they need to move in and out of tissues and into blood vessels to patrol, clear pathogens and/ or collect antigens followed by entering lymph vessels and migrating towards lymph nodes to interact with T cells and B cells [74]. To perform these functions, there are two actions that macrophages are engaging in- migration or transmigration (entering tissues) which essentially is macrophages squeezing through

endothelial pores [76]. Transwell assays or Boyden chamber assays are a valuable tool to study this migration and invasion of cells[76]. The assays contain a chamber divided into two compartments by a porous membrane. Cells whose migration is to be tested is placed in the upper compartment and a chemoattractant are placed in the lower compartment. There are multiple transwell assays available with different pore sizes. In this study, we used 3 µm sized pores (Corning, catalog# CLS3415). As a chemoattractant, we used the 4T1 breast cancer cell line that is characterized by high RAW264.7 macrophage infiltration [77]. Hence, in the bottom chamber, 2×10^5 4T1 cells were seeded in 6 wells overnight and RPMI were added to 6 other wells as control. MB-MΦ and MΦ were then seeded in the upper chamber at a density of 2×10^3 cells. Setup illustrated in Figure 8 below.

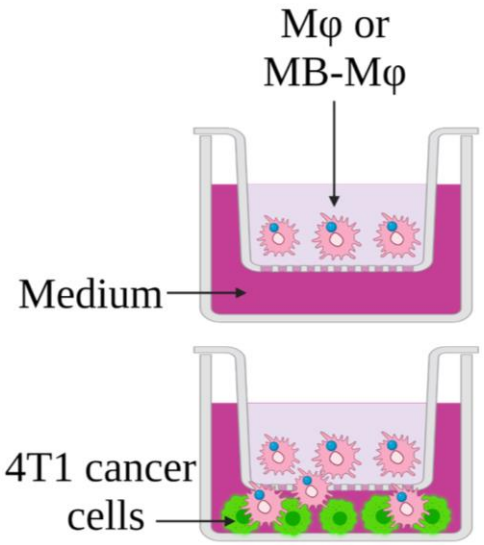

Figure 8: Setup to assess functionality of labeled MB-MΦ *in vitro*

Since our objective was to see if labeling affected ability to migrate, we used the lower end of the typical 12-22 hour range that many studies use and in keeping with our suggested

time window for labeled cells [48], [78], [79]. After 12 hours of incubation, we removed the upper inserts. No further labeling or staining was required in this study as we used MΦ expressing mCherry and 4T1-Fluc-Neo/eGFP-Puro cells expressing firefly luciferase which were obtained from Imanis Life Sciences. Using 20x fluorescent microscopy we assessed the number of migrated MΦ and MB-MΦ in the presence or absence of cancer cells. In the absence of 4T1 breast cancer cells, we observed no significant migration in MΦ ($p>0.9999$) regardless if they were labeled with MBs or not. However, In the presence of 4T1 cancer cells, a significant number ($p<0.0001$) of MΦ and MB- MΦ migrated, again, with no significant differences ($p=0.9164$) in their migratory capability. Here our finding suggests that MB labeling does not affect their innate ability to migrate.

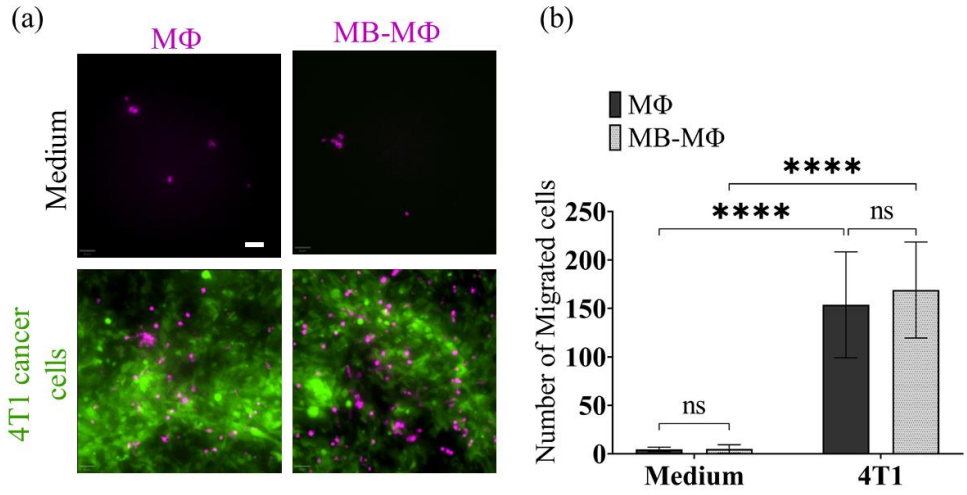

Figure 9 : MB-MΦ retain migratory capability *in vitro.*
MΦ and MB- MΦ were tested for their migratory capability via boyden chamber assay. (d) Representative microscopy images where 4T1 cancer cells are in green and MΦ and MB-MΦ in pink. Scale bar 50 μm. (e) Quantitative analysis of number of migrated MΦ and MB- MΦ in presence and absence of 4T1 cells. No significant differences were observed in migratory capability of macrophages when labeled with MB Thus indicative of labeling

not affecting innate functionality. P values were determined by two-way ANOVA, Tukey's multiple comparisons test. (Prism 9; GraphPad). ****P < 0.0001; n.s. - not significant.

At this juncture, we have established that the MB-MΦ exhibit high echogenicity and remain viable under clinically relevant ultrasound exposure conditions. Furthermore, they preserve their inherent ability to migrate irrespective of the labeling process. In the next chapter, we will explore whether these MB-MΦ produce detectable US contrast *in vitro*.

CHAPTER 3. IMAGING MB-MΦ WITH US *IN VITRO*

3.1 Assess US contrast of MB-MΦ

We hypothesized that the MB-MΦ needs to be labeled with at least one MB to produce contrast and to be detectable with US. Given that our earlier results indicated that at least 90% of the cells were successfully labeled, we anticipated a robust signal. To test this hypothesis, we opted to employ compounded B-Mode imaging. B-Mode imaging which is routinely used in clinics, generates two-dimensional (2D) grayscale images of the internal structures of the body. The term "B" in B-Mode stands for "brightness." The brightness of each pixel in the image corresponds to the intensity or amplitude of the ultrasound echoes received by the transducer. This received echo is a culmination of both scattering and reflection phenomena. Implementing spatial compounding, which is essentially several US images are taken from slightly different angles and then averaged to form a single image has two distinct advantages over conventional B-Mode. Firstly, spatial compounding is instrumental in attenuating speckle noise, which is spatially invariant and is dependent on the angle of incidence. By capturing images from multiple angles and subsequently averaging them, spatial compounding can reduce this type of noise, further bolstering the image quality. Secondly, some tissue structures may reflect the US beam better at certain angles. Thus, taking images from different angles can improve the visibility of these structures.

In order to assess US contrast, the harvested MΦ and MB-MΦ were injected into a hollow chamber of diameter 1.6 mm in an acoustically transparent phantom made of 12% gelatin w/v (APPENDIX B. Tissue mimicking phantom). They were then imaged using

the L22-14v linear array transducer (Vermon, France) connected to a programmable ultrasound scanner (Verasonics Vantage). This transducer has an elevational beamwidth of 1.6 mm and hence the total sonicated volume was 3.2 µl. The cells (which were at a notably high concentration of 10^6 cells/ ml) were consequently made to flow at a rate of 10 µl /s such that each frame had a fresh set of cells.

Regarding the imaging strategy, we employed a compounded B-Mode imaging paradigm with 7 angles between -0.3º and +0.3º and imaged at 18 MHz. (center frequency). Pulse width of 0.67, 4 half cycles and positive starting polarity were other parameters used to configure the transmit/ excitation waveform. To maintain consistency with previously reported viability values and MI window, we sought to convert all the pressures from Verasonics to MI. The MI was determined using a calibrated hydrophone (Onda, Sunnyvale, CA, USA) with a reported uncertainty of ±10% in the frequency range of the excitation. The MI exhibited values within the range of 0.08 to 0.9, corresponding to driving voltages spanning from 3 to 30 volts. These results are presented below in Figure 10.

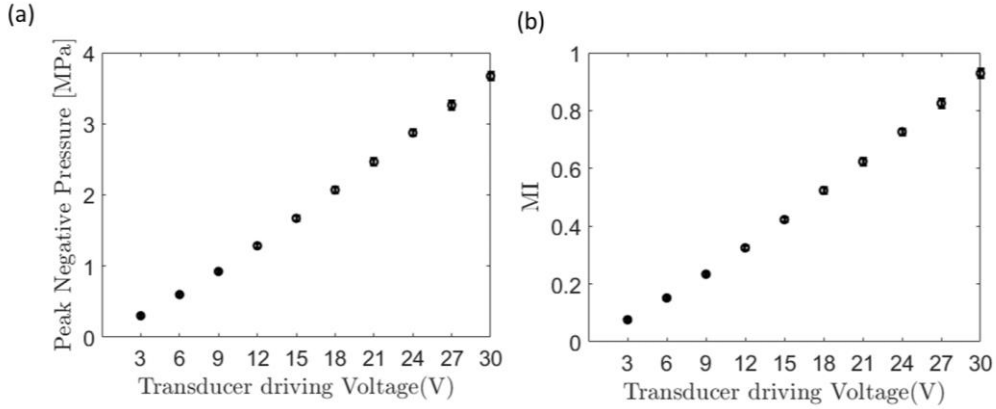

Figure 10: Mechanical Index derivation for L22-14V Transducer with Verasonics Vantage 256.
a) Peak negative pressure in MPa for the input voltages employed (b) Subsequent Mechanical Index or MI for the input voltages employed.

On sonicating the MΦ and MB-MΦ, it was observed that the MB-MΦ produced robust and distinguishable contrast even at a low MI of 0.08 (Figure 11b). Intriguingly, on further increasing the MI, even the MΦ produced strong contrast which could be expected as the incident pressure, P_i is increasing ($\sigma s \propto P_i; Equation\ 5$)

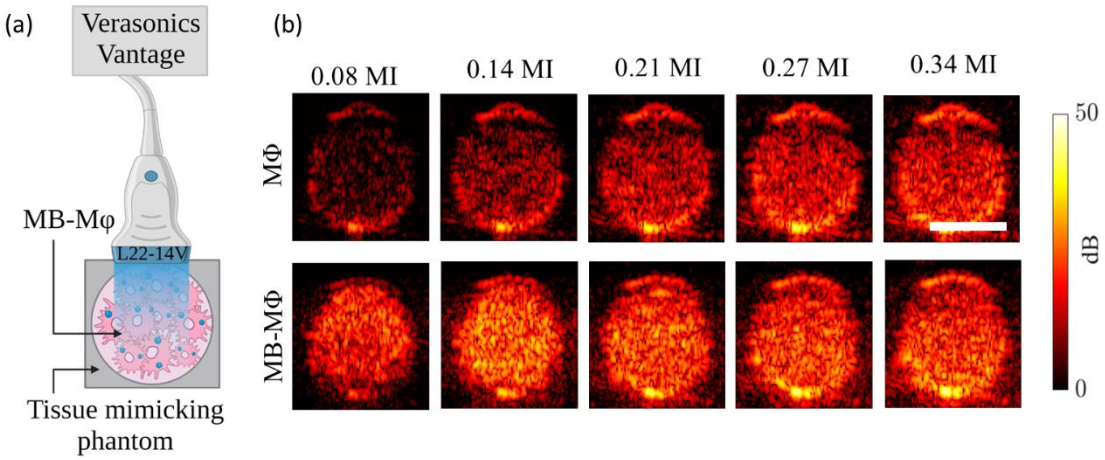

Figure 11: MB-MΦ has high contrast in vitro with B-Mode at low MI.

(a) Setup to image MB-MΦ and MΦ (control) in a tissue mimicking phantom made of gelatin via ultrasound. (b) Representative ultrasound images of MB-MΦ and MΦ acquired using B-Mode at varying MI showing high contrast of MB-MΦ at low MI. Scale bar 1mm

3.2 Increasing specificity of MB-MΦ

Building on the findings from the previous section, where we succeeded in generating contrast in the MB-MΦ labeled at lower pressures, it was evident that specificity declined with increasing pressure. Given that MΦ labeled with MBs exhibit non-linear properties, this section of our study aims to leverage this non-linearity. The renowned

Rayleigh-Plesset equation given below describes the radial oscillations of a MB under an acoustic field[80].

$$\ddot{R}R + \frac{3}{2}\dot{R}^2 = \frac{1}{\rho_o}\left[\left(P_V - P_0 - \frac{2\sigma}{R}\right)\left(\frac{R_0}{R}\right)^{3k} - 4\mu_L\frac{\dot{R}}{R} - \left(P_V - P_0 - \frac{2\sigma}{R}\right) - P_{ac}(t)\right] \quad (9)$$

Where $R(t)$ is the radius of the MB, ρ_o Is the density of the fluid, P_V is the vapor pressure , P_0 is the hydrostatic pressure. $\frac{2\sigma}{R}$ is the surface tension and k is the ratio of specific heats. $4\mu_L\frac{\dot{R}}{R}$ is the viscous friction and P_{ac} refers to the incident acoustic pressure.

Even for small oscillations, where $R = R_0 + x; such\ that\ \frac{x}{R_0} \ll 1$, it can be demonstrated that nonlinear terms like $x\ddot{x}, \dot{x}^2, \dot{x}x$ are present.

$$\begin{aligned} R_0\ddot{x} + x\ddot{x} + \frac{3}{2}\dot{x}^2 &= \frac{1}{\rho_o}\left[P_V - P_0 - \frac{2\sigma}{R_0} + \frac{2\sigma x}{R_0^2} - P_V\frac{3kx}{R_0} + P_0\frac{3kx}{R_0}\right. \\ &+ \frac{2\sigma 3kx}{R_0^2} - \frac{2\sigma 3kx}{R_0^3} - 4\mu_L\frac{\dot{x}}{R_0} + 4\mu_L\frac{\dot{x}x}{R_0^2} - P_V + P_0 + \frac{2\sigma}{R_0} \\ &\left. - \frac{2\sigma x}{R_0^2} - P_{ac}(t)\right] \end{aligned} \quad (10)$$

The generation of these nonlinearities fundamentally stems from the fact that, in the most basic scenario, MBs can only compress to a certain limit, whereas their expansion is not inherently capped and can theoretically be infinite. An alternative perspective is that since the density of the gas within the microbubble increases during compression and decreases during expansion, this causes the motion of the bubble wall to be asymmetric in response to incident pressure. This notable observation paved the way for the development of harmonic imaging techniques [81], [82]. Figure 12 adapted from Morgan et al demonstrates this nonlinear oscillation of a 2.6 μm MB that could potentially be detected by transducers and separated from linear components like tissues [83]. Additionally, the study highlighted that the polarity of the transmitted pulse plays a role in the MB's behavior: a positive polarity causes the microbubble to contract, whereas a negative polarity leads to its expansion. This results in distinct frequency signatures depending on the polarity of the pulse as shown in Figure 12b.

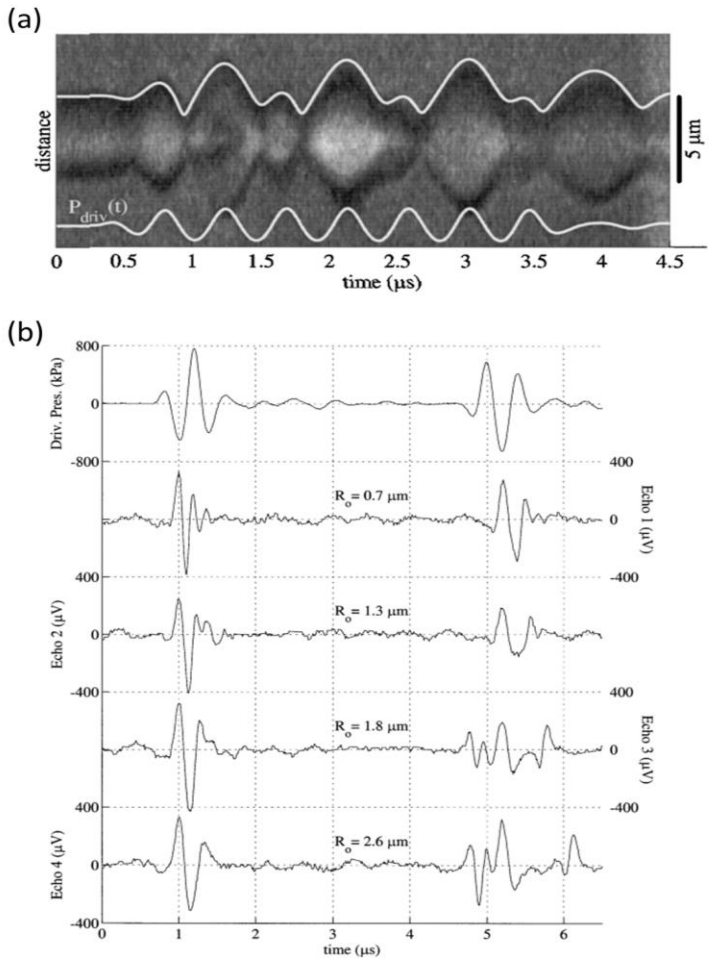

Figure 12:MBs can produce distinct non linear oscillations that are separable from linear components.

(a) A diameter-time streak image of a MB oscillating with a peak negative pressure of 360 kPa under 2.25 MHz pulse. The transmitted 7 cycle pulse is overlaid in white at the bottom and predicted radius is overlaid in grey. (b) comparison of the received echoes from bubbles of four varying sizes. The top trace represents a transmitted pulse pair (180° and 0° pulses) that are separated by 4 µs and have a peak negative pressure of 650 kPa. The second trace displays the echo received from a bubble with a radius of 0.7 µm, resulting from the transmission of this pair of pulses. The third trace shows the echo received from a 1.3-µm bubble, the fourth trace represents the echo from a 1.8-µm bubble, and the fifth trace captures the echo from a 2.6-µm bubble. It's notable that bubbles with different radii exhibit distinct received waveforms. Additionally, altering the pressure can yield comparable variations in the received echoes. Images adapted from Morgan et al [83].

It is important at this point to distinguish between orders of scattering and harmonics. First order scattering produces an amplitude scaled an amplitude scaled version of the incident pulse, hence it contains only the fundamental frequency (this is what linear scattered usually produce). Higher order scattering that gets more pronounced with increasing pressure introduces harmonics of the fundamental frequency. This concept is explained very well in the figure adapted from T.A Whittingham below[84]. Second order echo scattering (eg: $sin^2(\omega t)$) has none of the fundamental frequency but a component that is twice the fundamental frequency which shows up as a second harmonic in the frequency domain and a constant. In a similar manner, Third order scattering has a component that is both thrice the fundamental frequency and a component that is at the fundamental. This existence of fundamental for a third order scattering is the basis of the nonlinear detection method called Amplitude modulation or AM. This "nonlinear" fundamental is different from the fundamental produced due to linear scattering or first order scattering and only exist when nonlinear scattering takes place. It can also be seen in the same figure, how e2, is not sensitive to the polarity of the pulse. Hence when pulses of inverse polarities are transmitted, the sum of the received echoes effectively cancels out the fundamental frequency and odd harmonics. In contrast, the amplitude of the second harmonic and other even harmonics is doubled. This is another method to distinguish between non linear and linear scatterers and is the basis of the non linear imaging method called Pulse Inversion or PI.

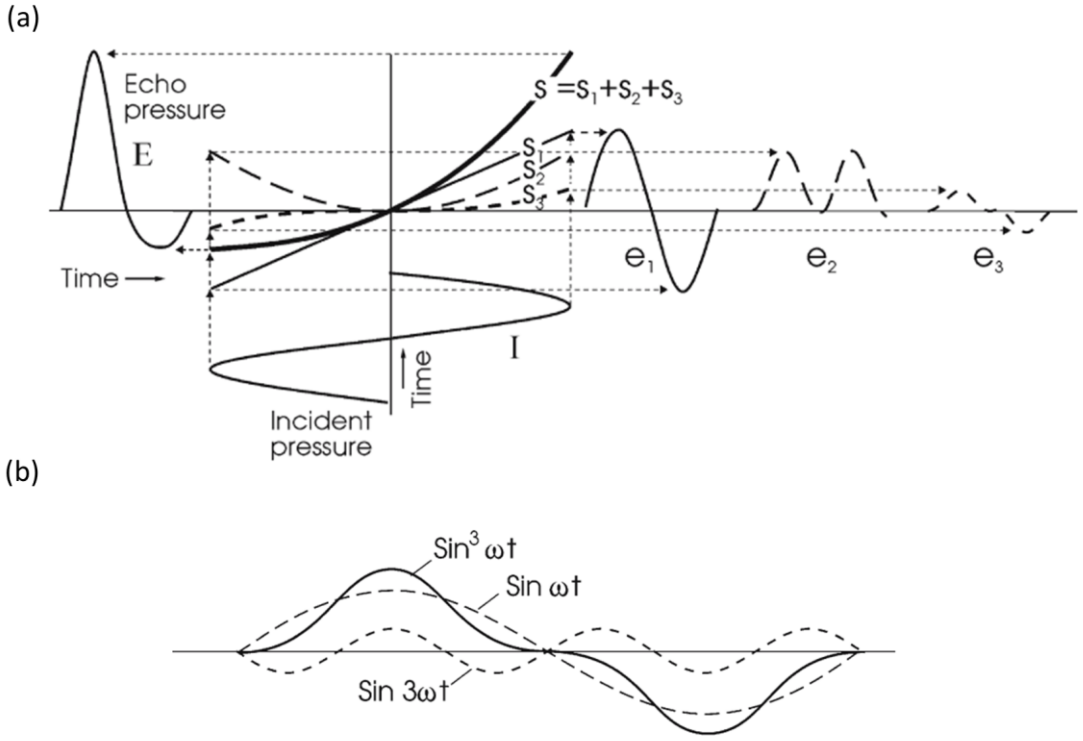

Figure 13: Orders of scattering versus harmonics

(a) Relationship between incident waveform (I) and scattered echo waveform (E) for a nonlinear scatterer. Curve S can be considered as the sum of the different orders of scattering produced (s1,s2,s3) and (e1,e2,e3) are the respective echoes produced due to scattering. E can be considered as the sum of e1,e2 and e3 . s1 is first order scattering and hence e1 is a scaled version of I. s2 is second order and is represented by a quadratic relationship; e2 therefore has twice the frequency and some scaling factor but most importantly no fundamental. Similarly, s3 is a cubic relationship had has both thrice the frequency and the fundamental in e3. This fundamental in e3 is different from the fundamental in e1. (b) Breakdown of e3 showing it is the sum of a component that is at the fundamental frequency and a third harmonic component.

There are hence two ways to detect MB signatures, AM and PI, each possessing distinct advantages as outlined in the literature [84]. PI, due to its ability to cancel the

fundamental frequency, has more specificity [85]. AM, on the contrary, has higher sensitivity due to preservation of some of the odd harmonics [86]. A combination of the two techniques, using three pulses (one full amplitude positive polarity and two half amplitude negative polarity), thus allows for increased contrast [86]–[89]. This technique will be referred to as Amplitude Modulation Pulse Inversion or AMPI and an illustration of this technique is given below in **Figure 14**. We will hence employ AMPI with the aim to enhance specificity.

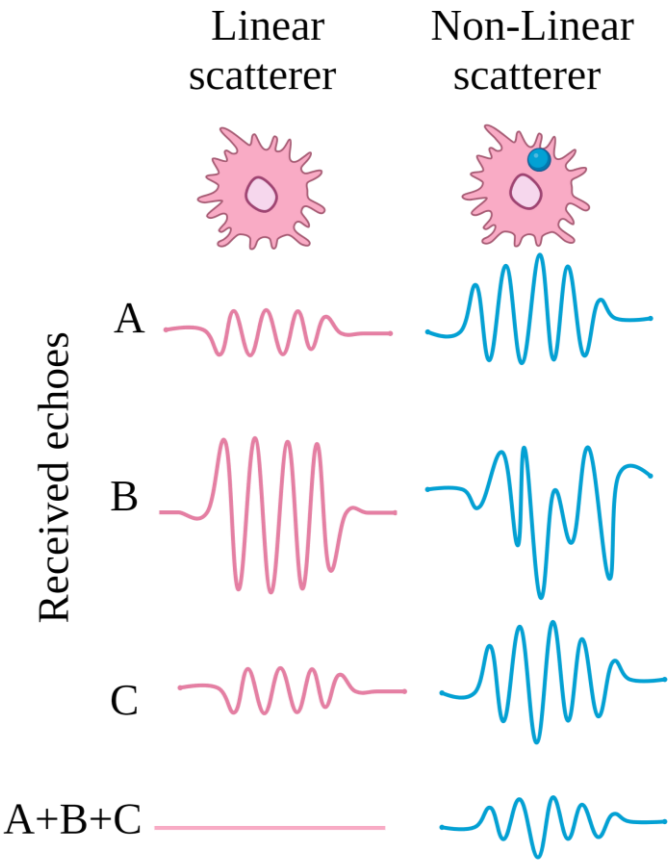

Figure 14: An illustration of the Amplitude Modulation Pulse Inversion (AMPI) technique.

Three pulses are transmitted – One of full amplitude and positive polarity and two of half amplitude and negative polarity. The received echoes from these transmissions are depicted here for a linear versus nonlinear scattered. A and C are half amplitude negative polarity pulses and B is a full amplitude, positive polarity pulse. In AMPI, the summation (A+B+C)

is displayed. Observe how for pulses A and C, the received echoes are higher for a nonlinear scatterer than that for a linear scatterer. AMPI, thus, has the advantage of receiving at fundamental yet being very specific to residue signal from MBs.

Using the same L22-14V transducer and Mechanical Index (MI) range as in earlier experiments, our goal was to image the MΦ and MB-MΦ within the tissue-mimicking phantom. We kept the same flow rate and concentration as before. We adjusted the sonication frequency from 18 MHz in B-Mode to 15.625 MHz in AMPI, a change necessitated by the hardware constraints of the Verasonics system which has a 62.5 MHz cap on the sampling rate (though it's worth noting there are methods to circumvent this via interleaving acquisitions, which we have not delved into in this thesis). Another default is that the signal be sampled at least 4 times the center frequency. Accurate sampling is critical for nonlinear imaging because it ensures that the signals are represented properly without loss of information, especially when dealing with high-frequency components like harmonics. With the default sampling rate and 4x requirements, the maximum center frequency usable is 15.625 MHz.

Consistent with our hypothesis, we successfully attained remarkable specificity using AMPI across all MIs tested, as depicted in **Figure 15**a. All acquired ultrasound images were subjected to log compression and displayed within a range of 0 to 50 dB to ensure uniformity and facilitate visual comparison. The reference image used were MΦ at 0.08 MI. The intensities of the images were determined using a circular region of interest (ROI) implemented in MATLAB. This approach was adopted to exclude the interface between the phantom and chamber, where there is an impedance mismatch that could introduce artifacts or distort the intensity measurements. The mean intensity values were

then calculated for three different sets of MΦ and MB-MΦ. Upon evaluating the signal intensities in **Figure 15**b, it was observed that AMPI generally exhibited elevated intensity levels relative to B-Mode for most of the MIs. However, at an MI of 0.08, the intensities were similar between the two modes. Notably, within the same plot, the intensity associated with MΦ is markedly low. This observation is particularly significant when interpreting **Figure 15**c, which highlights the enhanced contrast achieved for the MB-MΦ when employing AMPI. On the other hand, the contrast for MB-MΦ reduces with increasing MI when imaging with B-Mode. This data suggests that in the clinic where B-Mode is more readily available, it might be imperative to optimize the MI. In the context of our study, lower MIs, specifically 0.08 and 0.14, yield adequate and distinguishable contrast. Overall, this data supports the efficacy of AMPI in providing superior contrast in detecting MB-MΦ.

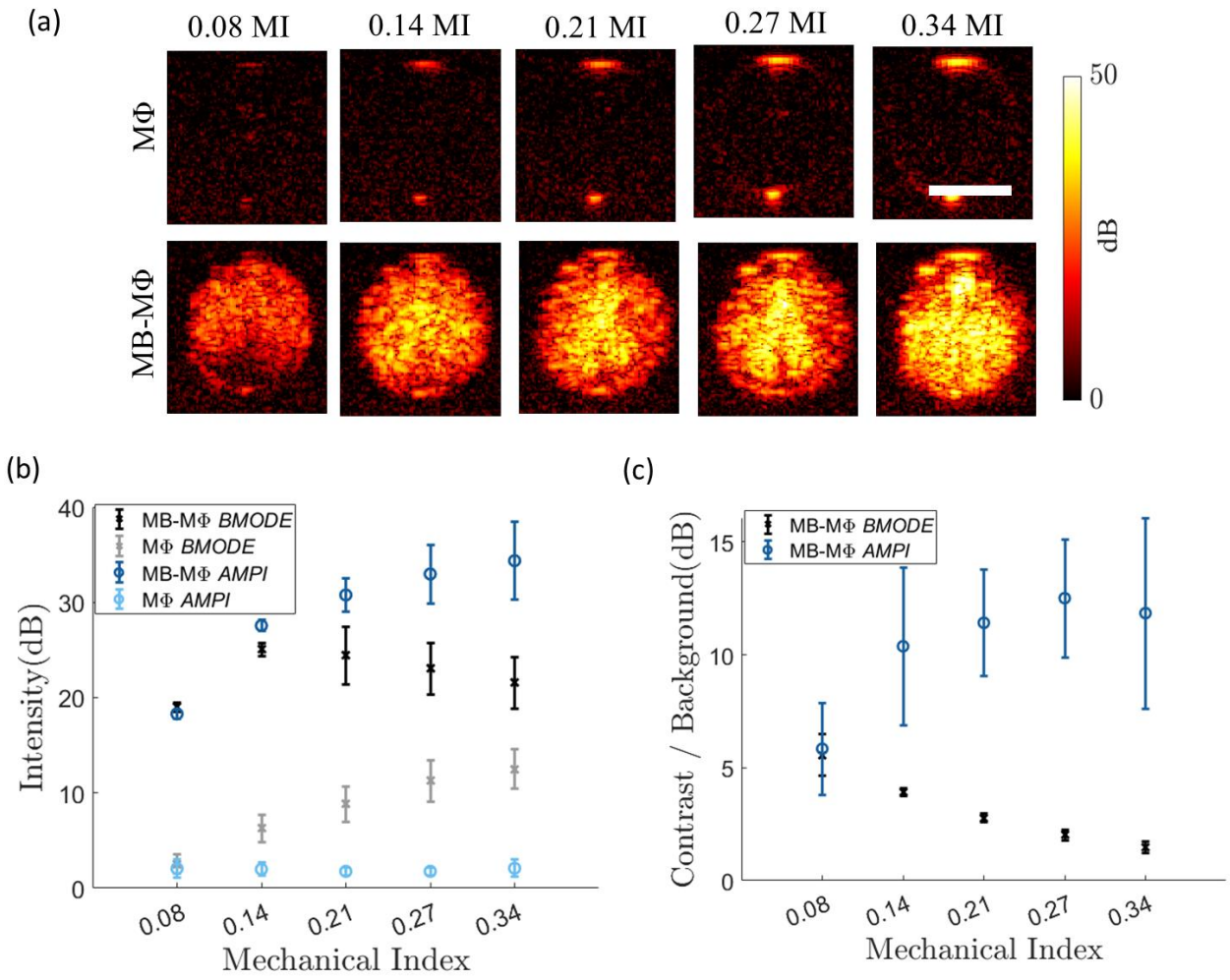

Figure 15: MB-MΦ has high specific contrast *in vitro* with AMPI

(a) Representative AMPI images of MB-MΦ and MΦ acquired using B-Mode at varying MI. Scale bar 1 mm. AMPI had a specific, high contrast for all MIs tested. (b) Quantification of the mean signal intensities observed in both B-Mode and AMPI at different MIs, indicating a pronounced intensity for the MB-MΦ with AMPI. It is particularly noteworthy that there is a consistently low intensity for the MΦ across all MIs. (c) Quantification of the contrast-to-background ratio of MB-MΦ using both methods at varying pressure levels, where the background is defined as the MΦ signal in both methods. Due to the observed low intensity of MΦ in AMPI, there is a notable increase in contrast. On the other hand, since the intensity for B-Mode increase with increasing intensity, the contrast reduces with increasing MI.

3.3 Persistence of contrast of MB-MΦ

While we were able to show robust contrast of MB-MΦ with AMPI and B-Mode (at lower pressures), it is imperative to evaluate the persistence of this contrast, as sustained contrast is essential for the longitudinal tracking of MB-MΦ. To this end, we administered a concentration of 10^6 cells/ml into a gelatin phantom, identical to the one employed in preceding experiments. Subsequently, two discrete Mechanical Indices (MIs), 0.08 and 0.14, were utilized, based on prior observations which indicated that they rendered distinguishable contrast in B-Mode imaging. We then observed a control volume without any flow for 1000 frames. Here since time is critical, we also ensured to equalize the time it takes for the entire sequence with B-Mode and AMPI considering their different acquisitions by adjusting the time in between frames.

Over the span of 1000 frames, B-Mode exhibited a consistent intensity as shown in Figure 16. In contrast, AMPI, displayed a decrease in contrast, which could be seen as both a function of the escalating MI and the increasing number of frames, as illustrated in Figure 16 a and c. This also gave more ground to sticking to these low MIs when imaging.

In summary, our investigation indicated persistence in contrast with B-Mode. While additional work is needed to clarify why AMPI leads to a decrease in persistence of the contrast, our data demonstrated how the selection of imaging sequence may be contingent upon the application. B-Mode, with its persistent contrast over time, may be a more conducive choice for longitudinal tracking. AMPI, due to its higher specificity, may be more favorable in scenarios characterized by high background signals.

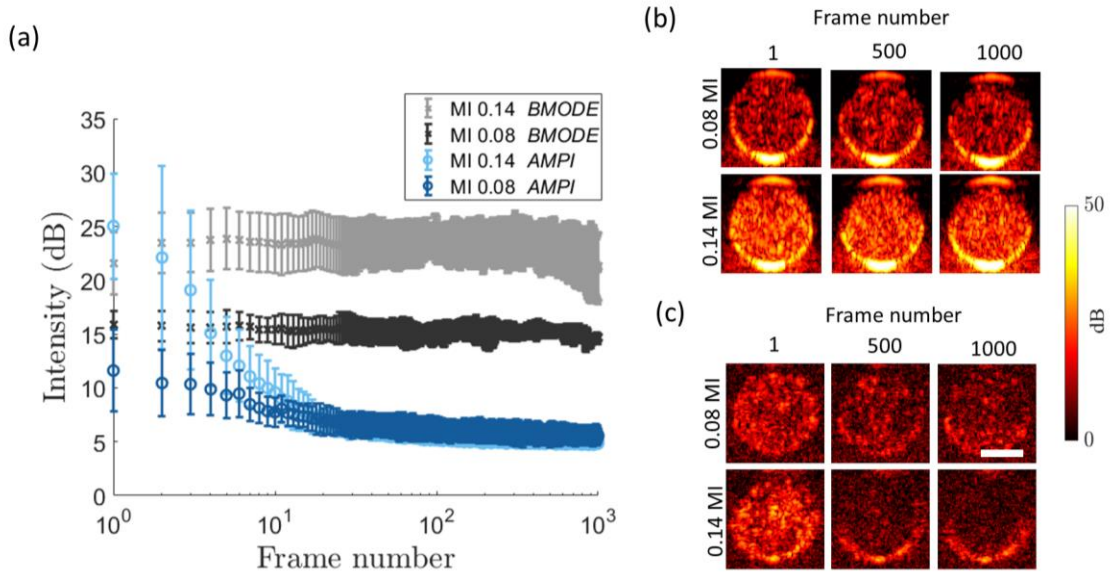

Figure 16: MB-MΦ has high persistency with B-Mode
(a) Intensity Quantification of signal across MIs 0.08 and 0.14 for B-Mode and AMPI, spanning frames 1 through 1000. (b) Representative B-Mode images captured at the initial frame, the 500th frame, and the 1000th frame, utilizing MIs of 0.08 and 0.14, providing a visualization of the consistent intensity over time. (c) Representative AMPI images at three critical time points: frame 1, frame 500, and frame 1000, utilizing MIs of 0.08 and 0.14, illustrating decrease in contrast with increasing MI and frames (exposure to US). Scale bar 1mm

3.4 Determine the detection limit of MB-MΦ *in vitro*

At this juncture, we have determined the MI (MI=0.14) that lead to the best imaging performance for both B-Mode and AMPI. Next, we will assess the detection limit to determine the sensitivity of our system.

To evaluate the detection limit, we imaged a progressively reducing concentration, from 10^6 to 10 cells/ml . It should be noted that, in our previous studies, we established that a concentration of 10^6 cells/ml yields robust contrast, hence serving as a good starting

point. The cell suspensions with varying concentrations were then injected into a tissue-mimicking phantom, similar to the one utilized before and imaged with both B-Mode and AMPI.

Consistent with previous results, 10^6 cells/ml produced a lot of bright echoes, showing the repeatability and reliability of this experiment. In the intermediate concentration range of 10^5 to 10^2 cells/ml, B-Mode imaging displayed a higher number of bright echoes compared to AMPI which could be attributed to contributions from unlabeled MΦs. Since the concentration for this experiment was assessed using an automatic cell counter (EVE™ Automated Cell Counter, NanoEnTek), there may be a possibility of injecting cells that are not labeled with MBs.

Finally, at the lowest concentration of 10 cells/ml, approximately 1-2 discernible spots were observed in both methods. With this phantom and the L22-14v transducer, the insonified volume is 3.2 µl. Given the random nature of cell distribution, there may be at most 10 frames where only 1 cell occupies the 3.2 µl volume, and those frames are represented in Figure 17. On plotting the point spread function (PSF) of the discernible spot, a full width half max of approximately 98 µm was obtained. This is the system's lateral resolution when operating at 15.625 MHz. With B-Mode, the lateral resolution was found to be 96 µm from the plot. This is slightly greater than the system's operational resolution at the same frequency, which is 86 µm.

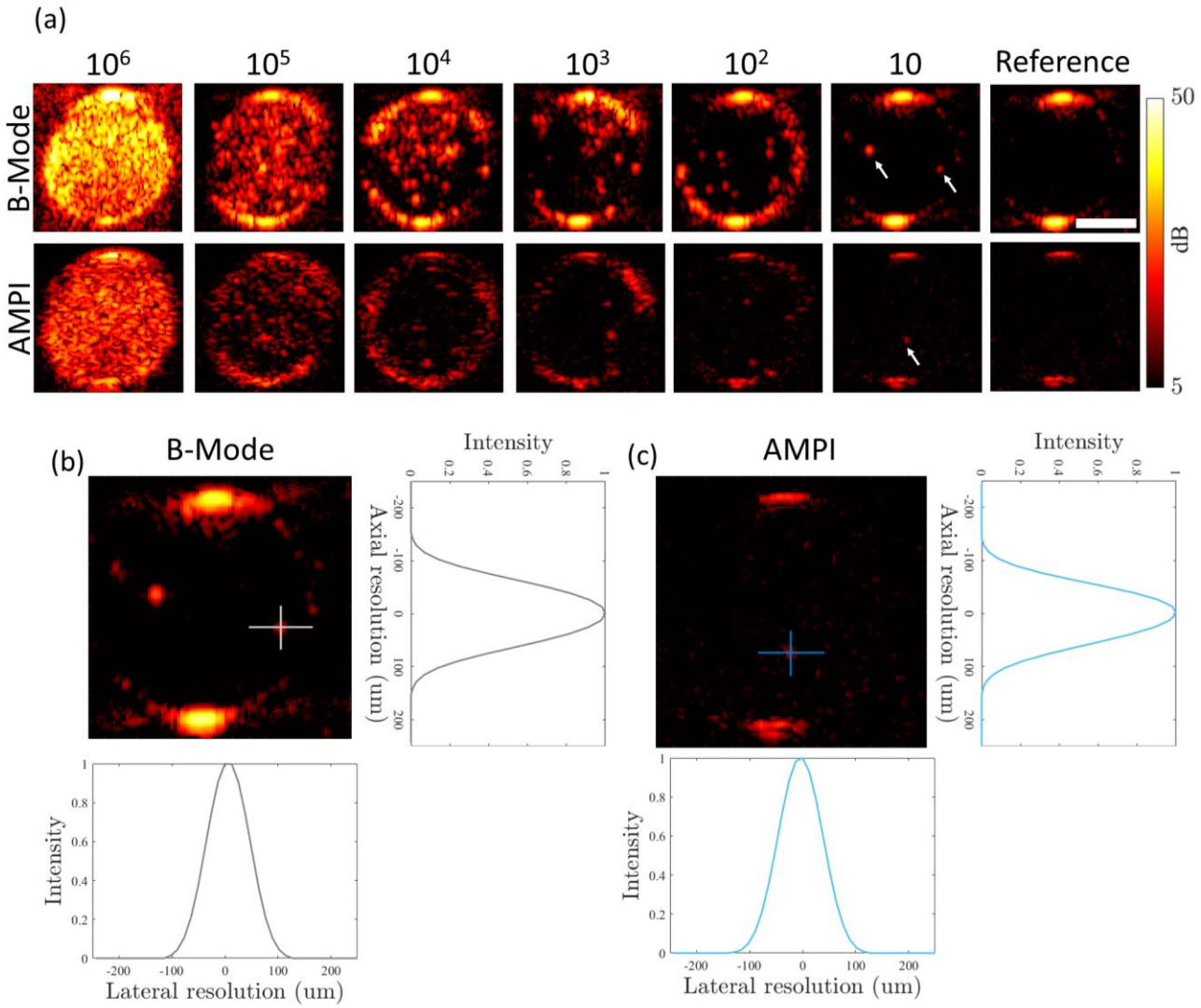

Figure 17 : High Sensitivity Detection with MB-MΦ and US *in vitro.*
(a)Representative B-Mode and AMPI images of different concentrations ranging between 10^6 MB-MΦ/ml to 10 MB-MΦ/ml. Both imaging techniques successfully discerned concentrations as low as 10 MB-MΦ/ml, highlighting their potential in applications necessitating high sensitivity, such as early cancer detection and the identification of micro metastases. Scale bar 1mm. (b) Lateral and axial resolution PSF of spot in B-Mode. (c) Lateral and axial PSF of spot in AMPI

In conclusion, the plotted PSF lends additional support to the possibility that US might be sensitive enough to detect a single cell. In summary, this experiment provides valuable insights into the sensitivity and detection limits of B-Mode and AMPI imaging

techniques in the context of cellular imaging. The ability to detect cellular concentrations down to 10 cells/ml holds promise for applications in which high sensitivity is important, such as in the early detection of cancer. A future work here could be quantifying the specificity and accuracy of both techniques, particularly at lower cell concentrations, to distinguish true signals from potential false positives. Our next step will involve assessing the performance of these imaging techniques in *in vivo* models which will be essential for their clinical translatability.

CHAPTER 4. IMAGING MB-MΦ WITH US *IN VIVO*

After identifying the US exposure conditions (MI=0.14), pulse sequences (B-mode and AMPI) capable of imaging MB-MΦ and determining their detection limit *in vitro*, we sought to test their imaging performance *in vivo*. To be able to relate the US image contrast with the number of cells present in the field of view we will directly infuse MΦ and MB-MΦ in 4T1 murine breast cancer grown in the flank.

Apart from offering the advantage of monitoring the cell count within the field of view, analyzing these cells' interactions within the tumor microenvironment can offer invaluable insights. These benefits extend beyond the basic ones such as confirming the dosage and location of delivery. For instance, a groundbreaking revelation was made when researchers demonstrated that T cells administered intrapleurally exhibited the ability to infiltrate, circulate, and persist at doses significantly lower than those typically employed in intravenous injections[97]. This discovery has thus opened new avenues in the ever-evolving field of cell therapies. Many current immunotherapies including Car-Macrophage based therapies have employed regional or intratumoral delivery[92], [93]. Studies indicate that these methods are well-tolerated by patients and may enhance the efficacy of the therapy [94]–[96].

While our ultimate goal remains systemic delivery, the understanding that tracking even intratumorally administered cells can provide significant benefits to current therapies is encouraging. This chapter aims to explore these aspects in greater depth.

4.1 Assess contrast of MB-MΦ *in vivo*

As we alluded to, macrophages need to have at least one MB in combination with US to distinguish them from cancer cells. To assess this, we used female Balb/C mice (The Jackson Laboratory) under protocols approved by the Institutional Animal Care and Use Committee at the Georgia Institute of Technology. To create a breast tumor model, we injected 10^6 4T1 cells subcutaneously into the posterior upper flanks of each mouse. 2 key decisions were made here: we selected the 4T1 tumor model as it is syngeneic to the RAW264.7 macrophage and displays high RAW264.7 macrophage infiltration [24]. Second, we opted for the upper flank to mitigate motion artifacts, particularly those that arise from respiration as this area can be taped down. The tumors were allowed to grow until they attained a diameter of at least 1.5 mm which typically occurred within a three-week timeframe post-inoculation.

At the time of the experiment, mice were maintained under 1.5% isoflurane anesthesia for the duration of the experiment on a temperature-controlled heat pad to maintain body temperature. The hair on the tumor was then removed via depilatory cream (Nair). This is necessary during US imaging for robust ultrasound coupling between transducer and skin. For US waves to penetrate into the tissue efficiently, it is essential to have good contact between the transducer and the skin. Hair can create air gaps, which are detrimental since ultrasound waves do not travel well through air. Following hair removal, a 25-G needle was inserted into the tumor which was connected to a syringe pump.

For imaging, we used the L22-14v transducer, consistent with previous experiments, which was connected to a Verasonics Vantage programmable ultrasound scanner. The

imaging plane was carefully aligned with the plane wherein the needle exhibited maximal intensity. MΦ/MB-MΦ were infused into the tumor at a rate of 100 µl/min over a duration of 2 minutes, with a concentration of 5×10^6 cells/ml. Figure below is a visual representation of the experimental setup accompanied by a depiction of the underlying hypothesis.

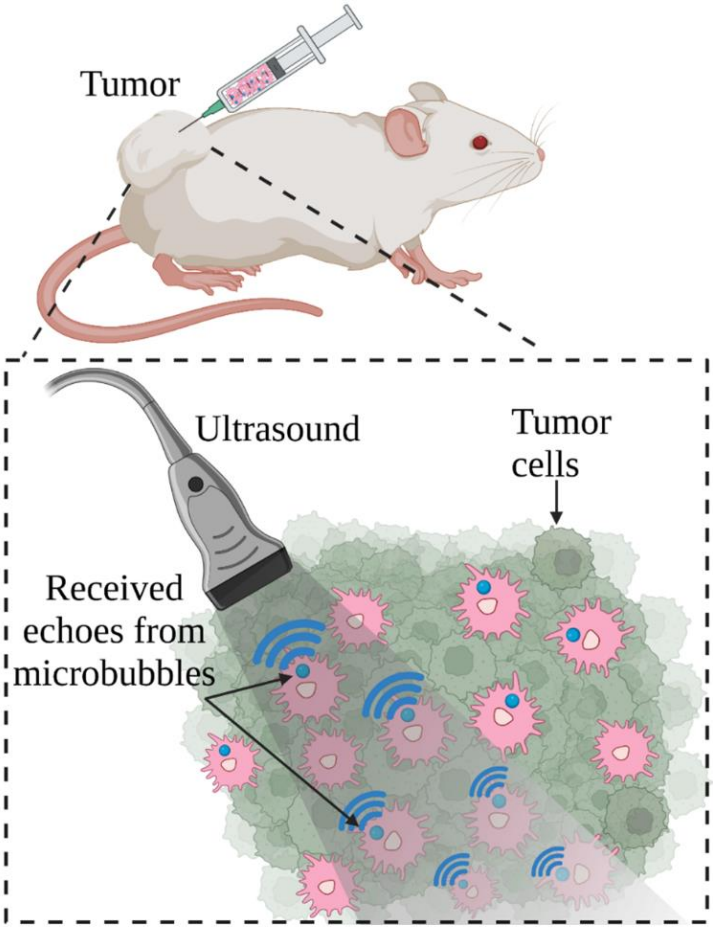

Figure 18: Experimental setup to assess the contrast of MB-MΦ in tumors via intratumoral injection.

We captured B-Mode images both before and after the infusion of MΦ and (MB-MΦ at the image plane where the needle intensity was at its peak, in order to monitor cell flow. We then created a maximum intensity projection from all the frames (~500 frames) encompassing the infusion period while removing background signal and it is presented in Figure 19. We then took an ROI within the tumor while avoiding the needle as shown in the quantification ROI in Figure 19a. We calculated mean intensity in dB. Histological examination confirmed the delivery of MΦ (Figure 19c, left) but there was no significant change in contrast before and after injection when the cells were not labeled with MBs ($p=0.3468$, $n=3$, Figure 19 a-b). However, when MB-MΦ were injected, a marked change in intensity was observed. These results thus underscore the importance of labeling MB-MΦ with MBs to distinguish them from surrounding cancer tissue.

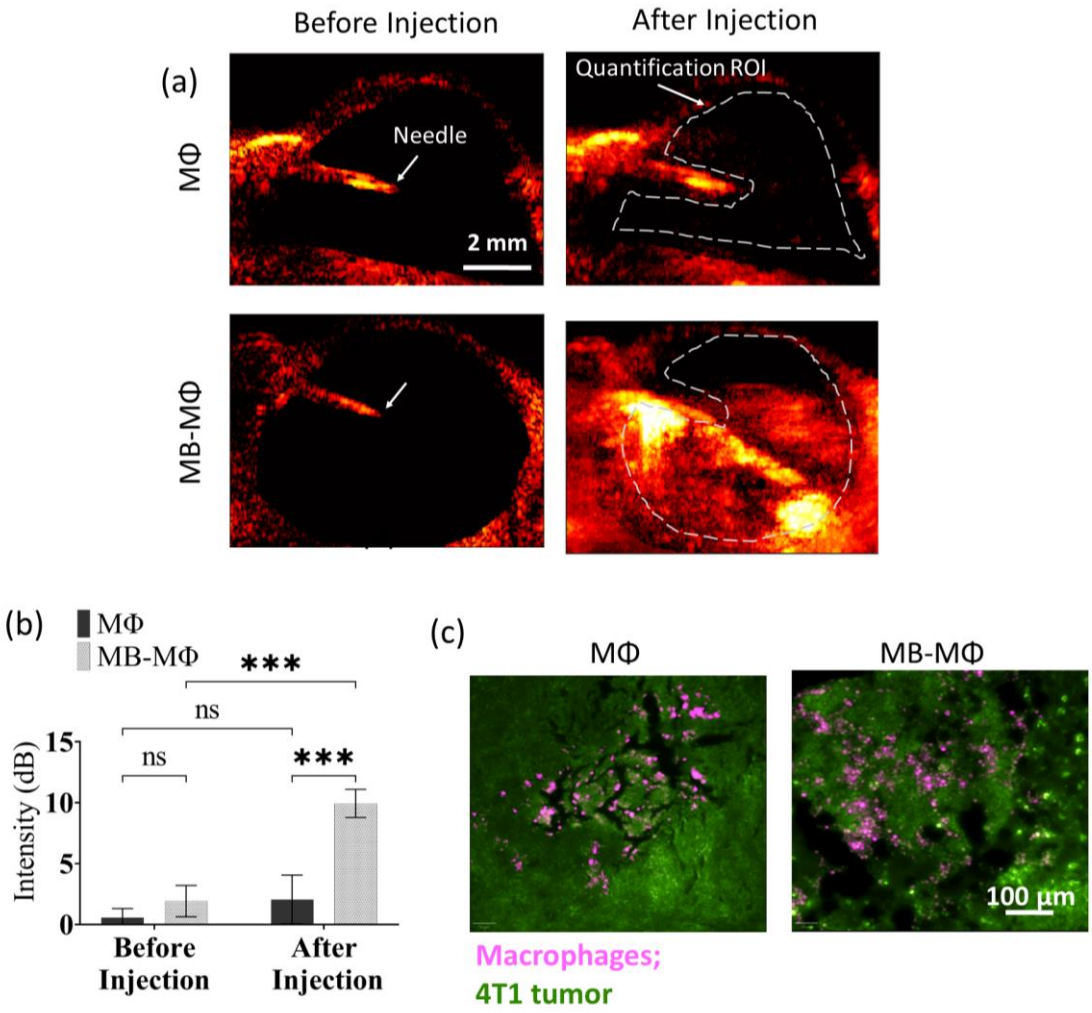

Figure 19 : MΦ produce high contrast when labeled with MB *in vivo*

(a) Maximum Intensity projections of *in vivo* B-Mode images of MΦ and MB-MΦ at the plane where the needle intensity was maximum for starting frame (before Injection) and last frame (after Injection). Arrows in before injection image point to the needle tip. Scale bar 2 mm b) Mean intensity calculated within ROI before and after injection of MΦ and MB-MΦ was assessed. While there was no significant change in intensity for the control (MΦ alone), a marked increase in intensity was observed when MΦ were labeled with MBs (MB-MΦ). c) Histological validation of delivery of MΦ and MB-MΦ (pink) to the tumor (green).

4.2 Persistence of contrast of MB-MΦ *in vivo*

A crucial element of this study involves determining the duration for which MB-MΦ can sustain contrast *in vivo*. This information is vital as it dictates the feasibility of longitudinally tracking cells over an extended period. To this end, we administered MB-MΦ intratumorally and imaged with B-Mode and AMPI. We specifically imaged at three time points- prior to the administration of MB-MΦ to establish a baseline, immediately subsequent to the injection to assess initial contrast, and at a later stage, specifically four hours post-injection, to evaluate the sustainability of contrast over time. We chose 4 hours, since we expected to see signal for this time window at least according to our results in Figure 2.

Given the importance of maintaining the longevity of injected MB-MΦ for the integrity of this study, we performed lymphodepletion. This well-established method essentially removes regulatory cells that may suppress the activity of the injected cells by attacking and killing them [96]. Specifically, a combination of cyclophosphamide (4 mg per mouse) and fludarabine (1 mg per mouse) was administered via intraperitoneal injection (i.p.) 18-20 hours before the introduction of macrophages and MB-macrophages. Cyclophosphamide (Cayman Chemicals, NDC 10019-955-01) was resuspended in sterile saline at 40 mg/ml immediately prior to use, and 4 mg per mouse was administered i.p. Fludarabine phosphate (Cayman Chemicals, NDC 25021-242-02, 25 mg/ml) was stored at 4ºC, and 1 mg per mouse was administered Intraperitoneally.

Consistent with previous results, we were able to see contrast right after injection in the tumor with both imaging methods. More remarkably, even at the four-hour mark, there was a noticeable persistence of strong echoes, indicative of sustained contrast. We took an ROI within the tumor and calculated intensities and presented the findings in Figure 20 b-c.

While a robust signal is visually apparent, there is an observable decrease in overall contrast. We hypothesize two potential explanations for this phenomenon. First, the MB-MΦ may have either exocytosed the MB or digested the MB, inline with our *in vitro* findings (Figure 2). The second proposition draws from studies indicating that T-cells injected regionally have the capacity to interact with cells, circulate and persist[90], [97] and similarly the MB-MΦ may have also left the injection site. While additional work is needed to investigate if the contrast reduction can be attributed to either MB loss or cellular interactions and consequent spread, the data demonstrates that the signal persists for at least 4 hours.

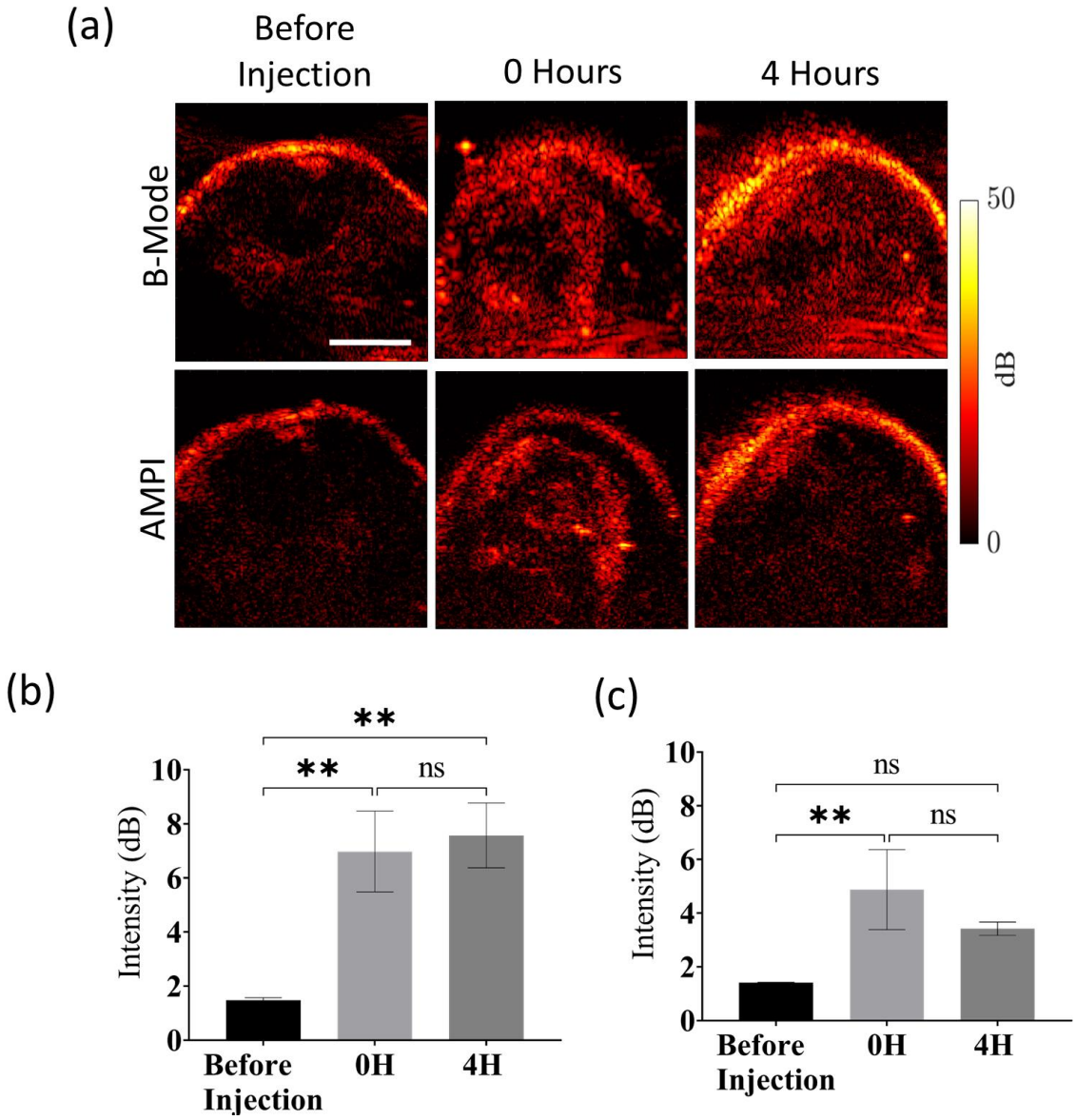

Figure 20: Persistence of contrast *in vivo.*

Representative B-Mode and AMPI images of MB-MΦ delivered intratumorally at three critical time points - before injection, immediately after injection, and 4 hours post-injection**.** The signal right after injection, at 0 hours, is consistent with previous results. At 4 hours, persistence of the contrast is still visible. Thus, underscoring a potential for longitudinal tracking of MB-MΦ in tumors. Scale bar 2 mm. (b) Quantification of intensity at the three time points for persistence of signal with B-Mode within the tumor (c) Quantification of intensity at the three time points for persistence of signal with AMPI within the tumor

4.3 Determine detection limit of MB-MΦ *in vivo*

We next sought to determine the lowest concentration of MB-MΦ detection limit *in vivo* that could be detected *in vivo*. Here, like our *in vitro* experiment, we varied the concentration from $10^5 - 10$ cells/ml. Since we already established that 10^6 cells produced robust contrast, we determined 10^5 cells/ml to be an appropriate starting point and varied the concentration to 10 cells/ml.

While maintaining the same setup as previous experiments with only concentration changing, we imaged with both B-Mode and AMPI. It was demonstrated that concentrations as low as 10 cells/ml could be readily detected *in vivo* with both methods as shown in Figure 21. Considering we inject 200 µl, this could theoretically allow for a ~2 cells to be administered into the tumor. This is a significant finding as it suggests that even a small number of MB-MΦ could be possibly tracked with high sensitivity, allowing for assessing and evaluating their behavior *in vivo*.

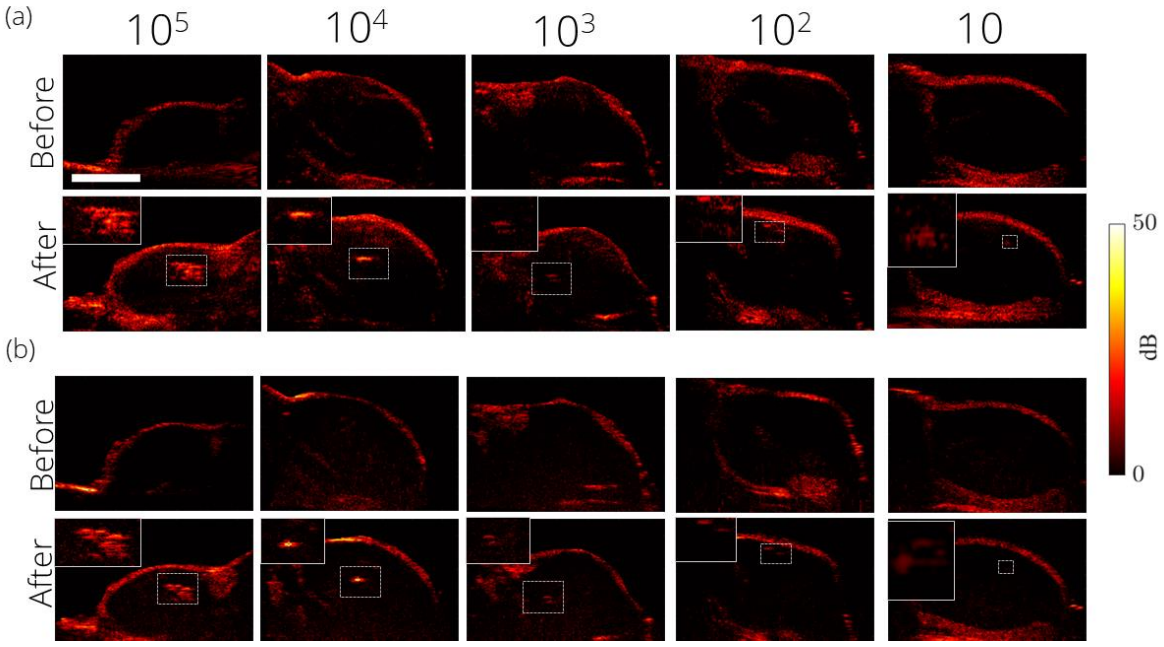

Figure 21: Detection limit of MB-MΦ *in vivo.*
Concentration of MB-MΦ was varied between $\mathbf{10^5 - 10}$ cells/ml. We were able to visualize as low as 10 cells/ml indicative of the high sensitivity of these MB-MΦ *in vivo*. Reference images were taken before each injection and needle placement, in both imaging modes- B-Mode and AMPI. These reference images are displayed in the top panel of both (a) and (b). White box in the 'after' images in both imaging modes highlights the region with the cells and the area zoomed into (a) Representative B-Mode images of the varying concentrations. (b) Representative AMPI images of the varying concentrations. Scale bar 2 mm.

4.4 Assess image guided delivery capability of MB-MΦ

As highlighted earlier, numerous clinical trials involving cell therapies employ the intratumoral injection of macrophages *in vivo*[95]. Nevertheless, for these therapies to be successful, it is crucial to confirm the accuracy of both the injection location and dosage to facilitate efficacious treatment and expedite clinical transition. The significance of employing a precise injection technique to avoid backflow has been well documented[100],

[101]. It is worth noting that backflow may be influenced by various factors including tissue pressure - which is typically elevated in tumors compared to surrounding tissues[102] - and the angle of the needle, among others. Taking these factors into account, we conducted an investigative experiment where we kept all other experimental parameters consistent (concentration, flow rate, needle gauge, tumor size) with the exception of the angle of injection, which was adjusted to a more horizontal position, thereby increasing the likelihood of backflow. Remarkably, this adjustment allowed us to visually observe the backflow of the MB-MΦ as shown in **Figure 22**. It is also noteworthy that this observation was made using B-Mode imaging, implying that the process does not necessitate any specialized algorithms, thus enhancing its translatability. Although we did not perform histological analysis to evaluate the residual MB-MΦ within the tumor, we observed a substantial number of MB-MΦ exiting the tumor. In both diagnosis and other cell therapies, where dosage precision is of the utmost importance and regulatory mandates constrain the quantity of cells, ensuring the delivery of the intended dose is vital for efficacy and subsequent clinical translation.

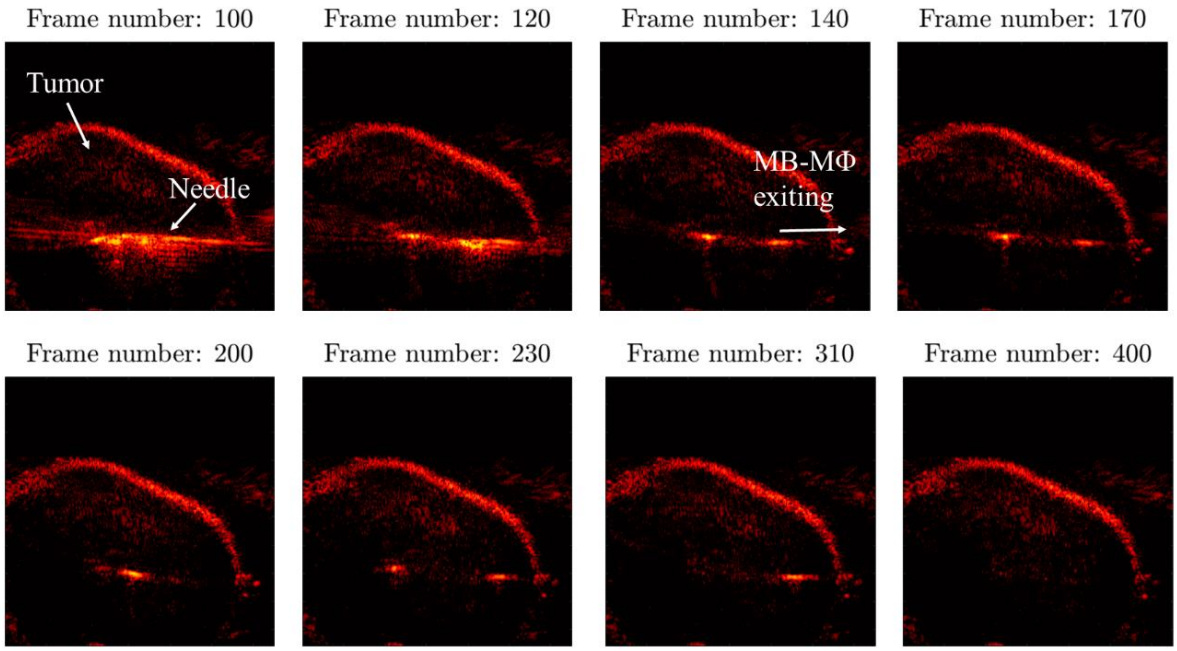

Figure 22: Investigation of MB-MΦ capability of image guided injections.

B-Mode frames showing MB-MΦ leaving the injection site. The ability to visualize and validate delivery of cell therapies is critical for their efficacy and subsequent translation. MB Labeling could be a potential gateway to visualize and track next generation cell therapies.

CHAPTER 5. IMAGE TRAFFICKING OF MB-MΦ TO BREAST CANCER

5.1 Assess tumor homing capability of MB-MΦ

In the previous chapter, we briefly discussed the remarkable ability of macrophages to not only target tumors but also penetrate them. In this chapter, we will evaluate the aptitude of the highly sensitive and echogenic MB-MΦ to migrate toward tumors upon systemic administration through tail vein injections. The underlying hypothesis and an illustration of this experiment are provided in Figure 23.

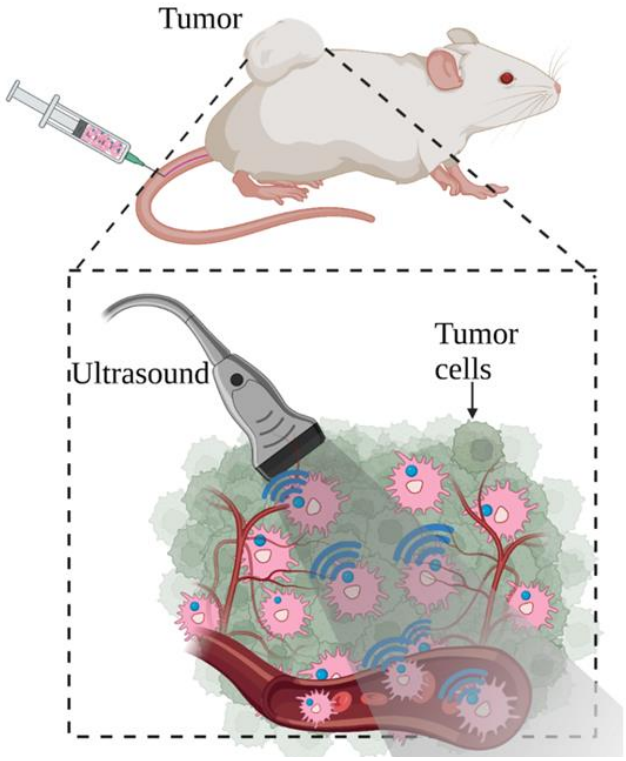

Figure 23: Experimental setup to assess tumor homing capability of MB-MΦ *in vivo.*

Because this is a systemic delivery, we had to increase the dose from the 10^6 cells/ml to 10^7 cells/ml. This increased dose is required because when cells are injected systemically, they are distributed throughout the entire circulatory system and consequently to numerous organs and tissues [101].

Our primary goal with this work is to build a diagnostic tool through these MB-MΦ. Macrophages can not only home towards tumors but also accumulate in them in proportion to the severity of the tumor [11]. The homing process and subsequent accumulation encompasses sensing the chemotactic gradient, adhesion to the endothelial lining of blood vessels near the tumor, extravasation (exit from the bloodstream), and migration through the tissue toward the tumor mass. This process can be on the order of hours and studies have shown that between 4-24 hours, significant signal is observed in tumor, liver and spleen [79], [102]. Hence in our study, we will employ the 4 hour time point. We also incorporated an 8 hour time point in this study to see if there is an increased accumulation. Our data from Figure 2 shows that there is sufficient labeling at this point.

We started with the same mouse model, BALB/c with an orthotopic 4T1 tumor. We also did lymphodepletion as before which is especially critical since this is a systemic injection. We injected the increased dosage and imaging with B-Mode and AMPI before and right after injection. We did not observe any signal immediately post injection within the tumor as some studies have reported [48]. Remarkably, in both AMPI and B-Mode, we saw a significant increase in intensity in the tumor at the 4 hour time point as shown in Figure 24 that plateaued thereafter demonstrating the ability of both linear and nonlinear US imaging to monitor macrophage flux and accumulation in solid tumors. We sacrificed

the animal at this point without perfusion such that we can assess density of MB-MΦ, particularly in the vessels and check for extravasation.

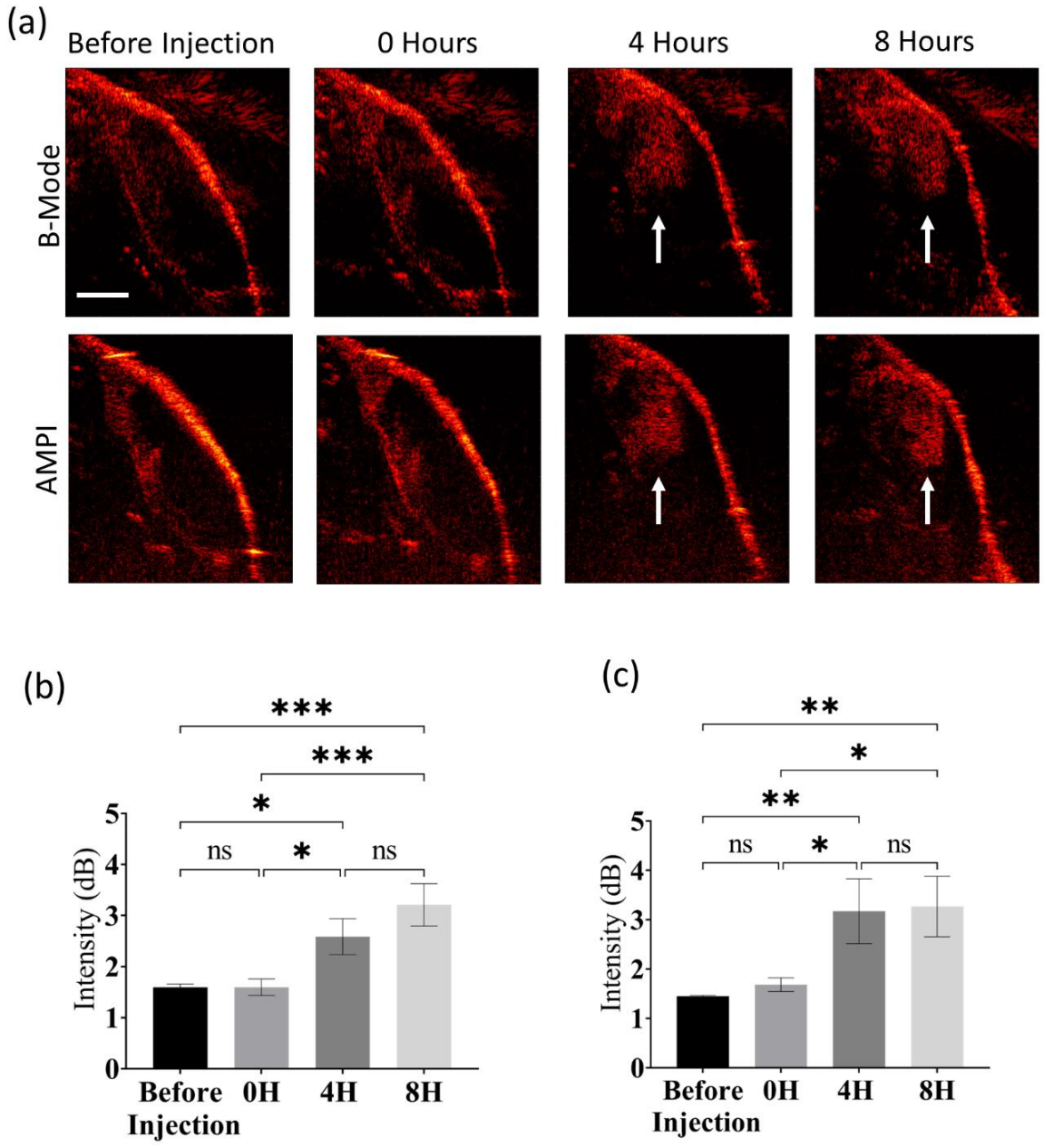

Figure 24 : MB-MΦ home towards tumors *in vivo*

(a) B-Mode and AMPI images of the tumor before injection, right after injection, 4 hours and 8 hours post injection. Signal within tumor is observed at 4 hours suggesting it takes several hours for MB-MΦ to reach tumors. Scale bar 2mm

5.2 Validation via immunofluorescence

In order to confirm if the observed signal in the previous section was from MB-MΦ, we harvested and sectioned the tumor according to the protocol detailed in APPENDIX C. Freezing and staining tissue . The tumor was sectioned into 20 μm thick slices. These slices were then subjected to staining for CD31, a protein also known as Platelet Endothelial Cell Adhesion Molecule-1 (PECAM-1). This protein, predominantly found on endothelial cells' surfaces, serves as an effective marker for blood vessels. Additionally, to visualize the cellular nuclei, the cells were stained with DAPI.

Upon imaging these sections using fluorescent microscopy, we were able to validate our hypothesis. The results affirmed that the US signals observed were indeed due to MB-MΦs. Moreover, the results also provided compelling evidence that MB-MΦs have the ability to extravasate from the vessels and infiltrate the tumor microenvironment (TME), underscoring their potential in diagnosing tumors. These are exciting results because most other US contrast agents even if functionalized to tumors cannot extravasate due to their size thus now giving us a potential avenue to image the trafficking and interactions of contrast agents with cancer via US.

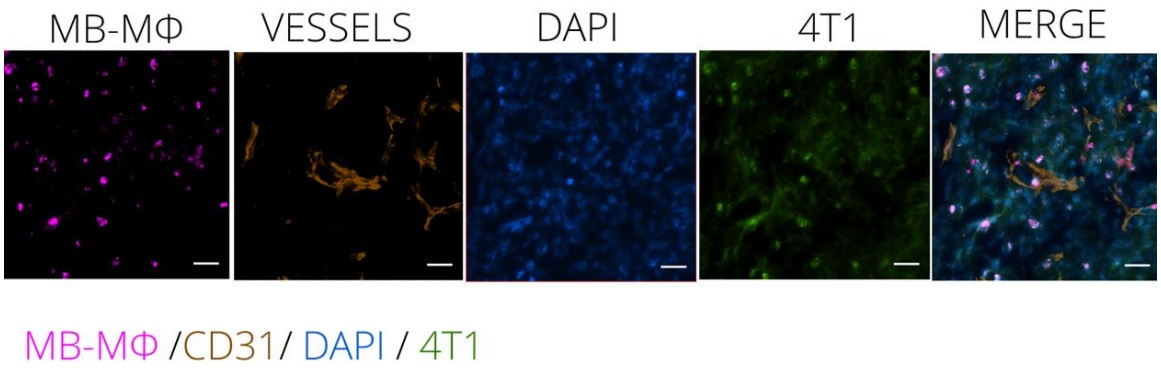

Figure 25 : Fluorescent images showing MB-MΦ accumulation and extravasation in the tumor 8 hours post intravenous administration.
Green signal is from tumor. Blue signal is from DAPI-labeled cells (nuclei). Brown signal is from CD31 (vessels) and pink signal is from injected MB-MΦ. Scale bar 10μm

5.3 Validation via Flow cytometry

To provide more quantitative assessment of the MB-MΦ we harvested the tumors as well as the spleen and liver and using flow cytometry we found that the tumor samples had the highest MB-MΦ to leukocyte ratio (30.6 ± 2.7 %) as compared to spleen (9.2 ± 0.6 %) and liver samples (4.8 ± 0.4 %). However, the tumor samples had the lowest viability with only 12.2 ± 1.4 % of live MB-MΦ, while the spleen and liver samples had viabilities of 87.5 ± 1.2 % and 74.0 ± 1.4 % of live MB-MΦ, respectively suggesting that the repeated US imaging might have negatively impacted the viability of the MB-MΦs that accumulated in the TME.

In a final interesting observation, we found that MB-MΦ originating from the disassociated tissue were still retaining the microbubbles (as depicted in Figure 26 c). This

not only served as a confirmation of the ultrasound signals in the tumors being produced by MB-MΦs, but also provided compelling evidence supporting the robustness and reliability of our proposed labeling approach.

Taken together with the insights from previous sections, these data demonstrate the ability of the MB-MΦ to travel through the vasculature, sense the tumor and penetrate the TME and provided evidence that this process can be tracked and quantified in real time with US. This understanding also opens up the prospect of considering MB-MΦs as smart contrast agents, given their ability to overcome the limitations of conventional ultrasound contrast agents, such as restricted circulation time (in minutes) and the inability to extravasate, therefore offering only vascular information [56].

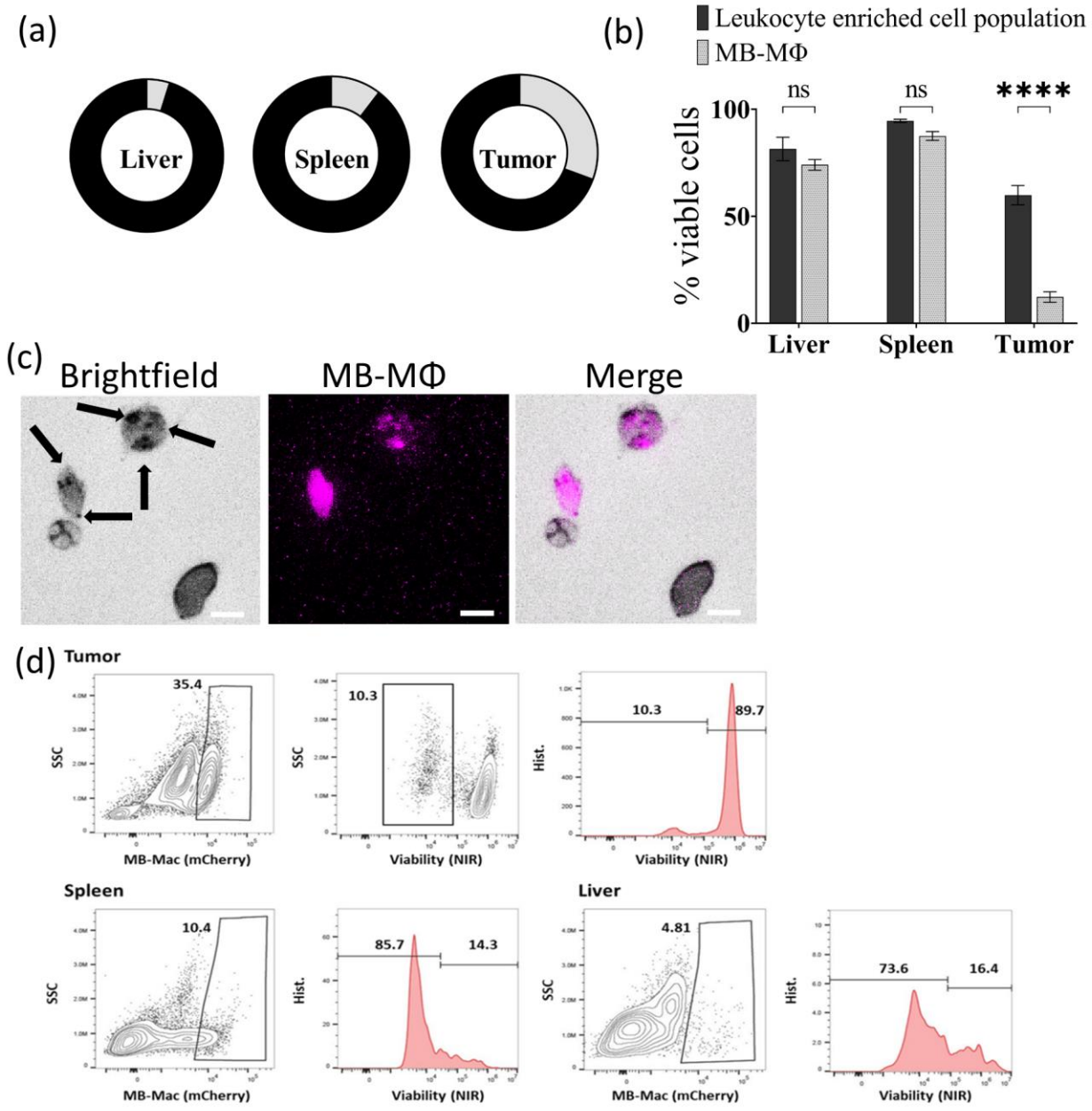

Figure 26: Validation via Flow cytometry

(a) Percentage of MB-MΦ to total leukocyte enriched cell population in Liver, spleen and tumor. (b) Viability of the MB-MΦ and total leukocyte enriched cell population in the liver, spleen, and tumor. (c) Microscopy images showing that MΦs (pink) retain the MBs (indicated by black arrows in brightfield) for at least up to 8 hours. Scale bar 10µm. (d) Representative plots obtained from flow cytometry for tumor, liver and spleen. P values were determined by one-way ANOVA, Tukey's multiple comparisons test (Prism 9; GraphPad). ****P<0.00001, ns- not significant.

CHAPTER 6. CONCLUSIONS, LIMITATIONS AND FUTURE WORK

6.1 Conclusions

In this study, we developed a robust technique for labeling macrophages with microbubbles, creating what we term MB-MΦ, without compromising on their migratory capabilities. Remarkably, MB-MΦ showed high echogenicity and maintained cell viability under an MI of less than 0.34, which is much lower than clinical limits. Using US imaging, we saw that MB-MΦ produced significant contrast and had an *in vitro* detection threshold as low as 10 cells/ml. Moreover, in an *in vivo* setting, MB-MΦ not only maintained high contrast for at least 4 hours post intratumoral injection but also demonstrated the ability to visualize concentrations as low as 10 cells/ml. Most impressively, we found that MB-MΦ could successfully home to and extravasate into tumors when administered through intravenous injection. Collectively, our data support the idea that echogenic macrophages could be used to track macrophage trafficking with high sensitivity, thus potentially serving as a viable and functional US imaging contrast agent.

6.2 Limitations

In the pursuit of scientific rigor, it is imperative to acknowledge the constraints and limitations inherent in any study. This section aims to address the various limitations that were encountered during this study. While every effort was made to ensure the validity and reliability of the research findings, it is important to recognize that these limitations may have an impact on the generalizability, applicability, or interpretation of the results. The

following subsections will detail each limitation and, where applicable, discuss how they might be addressed in future research.

6.2.1 Usage of non clinical frequencies

In our research investigations, we employed frequencies ranging from 15.625 to 18 MHz, which are higher than those typically utilized in clinical settings. Despite this disparity, our primary focus was on the scattering cross section and subsequent scattered power and we found that there was minimal variation observed in this specific parameter as shown in Table 3. Therefore, despite the disparity in frequency, our study's results and conclusions regarding the applicability of MB-MΦ as a viable US imaging contrast agent is still relevant. At lower frequencies which includes clinical frequencies and resonant frequency, the scattering should be much higher and hence produce better contrast. .

6.2.2 Lack of comparison to MB only in vivo

It is widely acknowledged that MBs in their basic form, do not possess inherent functionality and exhibit a limited lifespan due to their fast clearance when used as standalone contrast agents[103]. Therefore, in our study, we did not directly compare the performance of MBs to MB-MΦ in an *in vivo* setting. Conversely, phagocytosis could potentially decrease the effective scattering cross-section by damping the oscillation of the MB [104]

Hence this relationship between damping and scattering cross section for MB-MΦ needs to be explored further. This analysis can provide valuable insights into the behaviour

and characteristics of MBs when localized within cells, as opposed to their unbound state in the bloodstream.

6.2.3 Usage of RAW 264.7 instead of bone marrow derived macrophages

In our preliminary investigation, we employed the RAW 264.7 cell line, which is a macrophage like cell line [108]. While this cell line offers various advantages such as ease of culture, cost-effectiveness, and consistency, it is important to acknowledge its limitations. One of the drawbacks of using RAW 264.7 cells is that they may not fully capture the characteristics of bone marrow-derived macrophages/monocytes (BMDMs) [109].

BMDMs are primary cells extracted directly from the bone marrow and may possess distinct phagocytic or labelling capabilities and trafficking behaviours compared to the RAW 264.7 macrophage-like cell line. Moreover, harvesting BMDMs from syngeneic mice can also alleviate potential safety concerns and pave the way for translation[110]. Therefore, while RAW 264.7 cells can be beneficial for initial screenings and investigations, BMDMs might be more appropriate for comprehensive studies that require a closer representation of *in vivo* macrophage biology. Hence, repeating the study with BMDMs will address this limitation and may also draw new insights into BMDM vs RAW 264.7 macrophages, that could serve as an invaluable for other researchers.

6.2.4 Limited understanding of macrophage phenotypes

It is well established that Macrophages have excellent plasticity in response to different environmental cues and can express different phenotypes which can produce

various cytokines[111], [112]. The phenotypes can range between the two extremes - pro-inflammatory and classically activated (M1) macrophages and anti-inflammatory alternatively activated (M2) macrophages[113]. This activation occurs in response to environmental cues[114]. Exposure to bacterial components like lipopolysaccharide (LPS), specific Toll-like receptor (TLR) activators, and the Th1 cytokine interferon-gamma (IFNγ) drives macrophages towards the M1 activation state. M1 macrophages are involved in phagocytosis and the eradication of microbes, the elimination of tumor cells, antigen presentation to T cells to stimulate adaptive immunity, and the secretion of pro-inflammatory cytokines in abundance[115]. Conversely, the presence of Th2 and tumor-associated cytokines such as IL-4, IL-10, IL-13, transforming growth factor-beta (TGF-beta), or prostaglandin E2 (PGE2) fosters M2 macrophage polarization. M2 macrophages, once activated, contribute to tissue repair, angiogenesis, and the clearance of debris[116]. In this study, we have several processes including labeling, harvesting, injecting, and imaging (involving ultrasound exposure), and it may be critical to assess whether any of these processes induce a shift in the macrophage's state that could potentially impact the efficacy of the respective stages. In this study, we have several processes including labeling, harvesting, injecting, and imaging (involving ultrasound exposure), and it may be critical to assess whether any of these processes induce a shift in the macrophage's state that could potentially impact the efficacy of the respective stages. Therefore, incorporating a characterization at every stage could help mitigate this limitation. As the macrophages in different states exhibit distinct surface markers - with M1 macrophages predominantly expressing CD80 and CD86, and M2 macrophages characteristically displaying CD163,

CD206 (mannose receptor), and CD204 - flow cytometry can be employed to evaluate their polarization[117].

6.3 Future work

6.3.1 Assess ability of MB-MΦ to detect micro metastasis and response to treatment.

It is well established that accumulation of macrophages is directly proportional to the severity of the tumour[11]. Moreover, it has also been shown that the presence of micro metastases, which often go undetected, can lead to the ineffectiveness of initial treatments[118] . A potential avenue for future research could involve examining the correlation between the accumulation of MB-MΦ in tumours of different sizes to aid in their detection. In particular to the desire to assess response to treatment, sensitivity to decreasing accumulation could be assessed. Work along the same lines using engineered macrophages were able to detect tumour volumes of 25-50 mm^3 using PET[119]. However, with US, we have the additional capability of getting more spatial resolution, which is lacking with PET [15] and potential to do more frequent imaging (due to its non ionizing nature) to really establish this as a diagnostic tool.

6.3.2 Imaging MB-MΦ trafficking at single cell resolution.

Effective imaging of macrophage trafficking is ultimately dependent on our ability to track individual cells as they interact with the host, including crawling and adherence to the endothelial cells followed by infiltration and transmigration into the tissue. However, to resolve this coordinated biological process in deep seated organs, challenges in imaging of macrophage trafficking at a single-cell resolution must be overcome. In the future, we will establish a super resolution framework for imaging MB-MΦ trafficking at single-cell

resolution. It was recently shown that by employing concepts originally developed in optical microscopy [120] to ultrasound in combination with microbubbles tradeoffs between resolution and penetration depth can be alleviated [121], [122]. Based on these methods, microbubbles that act as (moving) sono-activatable sources are localized one by one with a precision far beyond the diffraction limit by localizing the signal from each microbubble in each frame (for example, by picking centroid of each diffracted microbubble signal[123]). Superimposing all the localized points to form density maps of USCA positions allows to resolve the microvascular "fingerprint" of organs with subwavelength resolution [124]. Resolution below 30 μm has been consistently reported across several studies in healthy and diseased rodents using research or clinical ultrasound scanners [123]. In most cases, the reported resolution (10-40 μm) is an order of magnitude below the diffraction limit [125]. Moreover, by tracking the same bubble as it flows through the vessel in consecutive frames the microvascular flow velocity can be determined (u=dx/dt). Termed super resolution ultrasound (SR-US) due to extended signal and image post-processing, this technique, which has a theoretically-achievable resolution on the order of a few microns for clinical ultrasound frequencies [123]. As a result, this approach opens up the potential to image the trafficking of MB-MΦs at a single-cell resolution.

The first step to achieve this would be to optimize parameters such MB-MΦ concentration, admission rate and frame rate which are critical parameters attaining resolution 10-fold beyond the diffraction limit and accurate velocity estimates. [127]. On the processing side, we have previously shown how morphological reconstruction improves micro vessel mapping [128] . This is particularly useful in the case of MB-MΦ

as it can alleviate issues that traditional SR-US algorithms where it ignores signals below some peak threshold. Since tumours are heterogeneous [129], there may be microbubble labeled macrophages in some vasculature that, may not produce a strong signal due to higher damping by vessel wall and hence eliminating these signals, might not give us the complete picture of trafficking (at single cell resolution) we are looking for. Additionally, conventional SR algorithms typically employ SVD (Singular Value Decomposition) filtering to exclude tissue signals by filtering out slow-moving objects [127]. However, in contrast to MBs in blood flow, MB-MΦ move at a significantly slower pace near tumor sites as they try to extravasate (<10 μm/hour) [130]. Therefore, adopting a non-linear approach like AMPI, which has already been employed in this thesis, might be instrumental in circumventing this limitation. For ultrasound frequency of 15.25 MHz (AMPI) and aperture of 27.3 mm, the lateral resolution, at imaging depth of 10 mm, is approximately 53.2 μm using ultrasound imaging. With SR-US imaging, we expect to attain effective resolution 5-fold below these diffraction limits, resulting in ~ 10 μm resolution. These limits will allow us to image MB-MΦ trafficking in tumor microenvironment at single-cell resolution. Additionally, incorporating velocity data may further enhance our ability to extract more prognostic information.

APPENDIX A. LINEARIZED BUBBLE THEORY

Starting with the well known Rayleigh Plesset equation

$$\ddot{R}R + \frac{3}{2}\dot{R}^2 = \frac{1}{\rho_o}\left[\left(P_V - P_0 - \frac{2\sigma}{R}\right)\left(\frac{R_0}{R}\right)^{3k} - 4\mu_L\frac{\dot{R}}{R} - \left(P_V - P_0 - \frac{2\sigma}{R}\right) - P_i(t)\right] \tag{11}$$

- $R(t) \rightarrow radius\ of\ microbubble$
- $\rho_o \rightarrow density\ of\ fluid$
- $P_V \rightarrow Vapor\ pressure$
- $P_0 \rightarrow Hydrostatic\ pressure$
- $\frac{2\sigma}{R} \rightarrow surface\ tension$
- $k \rightarrow ratio\ of\ specific\ heats; k = 1\ if\ isothermal$
- $4\mu_L\frac{\dot{R}}{R} \rightarrow viscous\ friction$
- $P_i \rightarrow Incident\ acoustic\ pressure$

For small sinusoidal excitation

$$R = R_0 + x; such\ that\ \frac{x}{R_0} \ll 1 \tag{12}$$

Equation 11 becomes

$$(R_0 + x)\ddot{x} + \frac{3}{2}\dot{x}^2$$

$$= \frac{1}{\rho_o}\left[\left(P_V - P_0 - \frac{2\sigma}{R_0 + x}\right)\left(\frac{R_0}{R_0 + x}\right)^{3k} - 4\mu_L \frac{\dot{x}}{R_0 + x}\right.$$

$$\left. - \left(P_V - P_0 - \frac{2\sigma}{R_0 + x}\right) - P_i\ (t)\right] \tag{13}$$

Expanding some terms in equation 13;

$$\frac{2\sigma}{R_0 + x} c\ \frac{2\sigma}{R_0}\left(1 - \frac{x}{R_0}\right) \tag{14}$$

$$4\mu_L \frac{\dot{x}}{R_0 + x} \approx 4\mu_L \frac{\dot{x}}{R_0}\left(1 - \frac{x}{R_0}\right) \tag{15}$$

$$\left(\frac{R_0}{R_0 + x}\right)^{3k} \approx 1 - \frac{3kx}{R_0} \tag{16}$$

Inputting Equations 14,15 and 16 in equation 13.

$$R_0\ddot{x} + x\ddot{x} + \frac{3}{2}\dot{x}^2$$

$$= \frac{1}{\rho_o}\left[P_V\ - P_0 - \frac{2\sigma}{R_0} + \frac{2\sigma x}{R_0^2} - P_V\ \frac{3kx}{R_0} + P_0\frac{3kx}{R_0}\right.$$

$$+ \frac{2\sigma 3kx}{R_0^2} - \frac{2\sigma 3kx}{R_0^3} - 4\mu_L\frac{\dot{x}}{R_0} + 4\mu_L\frac{\dot{x}x}{R_0^2} - P_V\ + P_0 + \frac{2\sigma}{R_0} \qquad (17)$$

$$\left. - \frac{2\sigma x}{R_0^2}\ - P_i\ (t)\right]$$

In this nonlinear approximation, we need to drop all nonlinear terms (basically, terms that cannot be separated like $x\ddot{x}, \dot{x}^2, \dot{x}x$); hence equation 17 becomes

$$R_0\ddot{x} = \frac{1}{\rho_o}\left[-P_V\ \frac{3kx}{R_0} + P_0\frac{3kx}{R_0} + \frac{2\sigma 3kx}{R_0^2} - \frac{2\sigma 3kx}{R_0^3} - 4\mu_L\frac{\dot{x}}{R_0}\ - P_i\ (t)\right] \qquad (18)$$

Rearranging equation 18

$$\ddot{x} + 4\mu_L\frac{\dot{x}}{R_0^2} + \frac{R_0(P_V\ - P_0 - 2\sigma) + 2\sigma}{R_0^3}3kx = \frac{[-P_i(t)]}{R_0\rho_o} \qquad (19)$$

Equation 19 can now be compared to a linear damped oscillator that takes the form

$$m\ddot{x} + \Upsilon\dot{x} + sx = forcing\ function \tag{20}$$

Where

$m = mass,$

$\Upsilon = damping,$

$s = spring\ constant$

Hence, resonant frequency can be given by;

$$f = \frac{1}{2\pi}\sqrt{\frac{s}{m}} \tag{21}$$

Notice how the L.H.S of equation 19 is very similar to equation 20. Hence by manipulating the R.H.S of equation 20, we can show that equation 19 is that of a linear damped oscillator.

Since we need force on R.H.S; let us multiply by $4\pi R_0^3\rho_o$ on both sides; hence equation 19 becomes-

$$4\pi R_0^3\rho_o\ddot{x} + 16\pi R_0\rho_o\mu_L\dot{x} + (R_0(P_V - P_0 - 2\sigma) + 2\sigma)12\pi\rho_o kx = F_{ac}(t) \tag{22}$$

Comparing equation 22 and 20; we can show that

$$f = \frac{1}{2\pi R_0}\sqrt{\frac{1}{\rho_0}\left(3k\left(P_V - P_0 - \frac{2\sigma}{R}\right) - \frac{2\sigma}{R}\right)} \quad (23)$$

$P_V = 0$ which is typical in biomedical application; and for $\sigma = 0$;

21 becomes;

$$f = \frac{1}{2\pi R_0}\sqrt{\frac{3kP_0}{\rho_0}} \quad (24)$$

24 is also known as the Minnaert Resonance frequency.

APPENDIX B. TISSUE MIMICKING PHANTOM

Materials-

1. Gelatin - 12g per 100ml
2. Degassed DI water - 300ml
3. Stir bars
4. Beaker (500ml capacity)
5. Hot plate
6. Mold with wire of the desired diameter for creating the hollow chamber.
7. Petroleum Jelly

Method-

1. Begin by heating the DI water in a microwave to 50°C. Place this on a hot plate to maintain the temperature. Position the stir bars in the water, setting them at a gentle and consistent speed to avoid causing agitation in the water.
2. Gradually sprinkle the gelatin into the water, continuing to stir with the stir bars. It's crucial to take this step slowly to prevent the formation of clumps.
3. Once the gelatin is fully dissolved and integrated into the water, transfer the solution to a vacuum pump to extract any trapped air bubbles. It's possible that some air bubbles will rise to the surface; if this occurs, stop the vacuum and gently skim off the top layer of the solution which contains these air bubbles. Repeat this process until you no longer observe any air bubbles in the solution.

4. Prior to pouring the gelatin solution, make sure to clean the wire in the mold with alcohol, and lubricate the mold with petroleum jelly for easy removal later on.
5. Carefully pour the gelatin mixture into your desired mold and place it in the refrigerator. Allow it to set at 4°C overnight before removing from mold and extracting wire.

Note: For optimal results and to avoid introducing impurities that might affect US imaging, it is essential to maintain a clean workspace and handle both ingredients and equipment with care.

APPENDIX C. FREEZING AND STAINING TISSUE

This protocol is for staining CD31 in 4T1 tumor tissue

Materials-

1. Paraformaldehyde (PFA)
2. 30% sucrose (30 g of sucrose in 100 ml DI water)
3. PBS
4. Isopentane
5. Dry ice
6. 5% Goat serum
7. 1% Bovine serum Albumin (BSA)
8. Primary antibody- Rabbit anti-mouse CD31 (AB28364)
9. Secondary antibody - Goat anti-Rabbit IgG Alexa Fluor™ 647 (Thermo fisher, A21245)
10. Mountant - Prolong Glass Antifade Mountant (Invitrogen , 2018752)
11. DAPI (Invitrogen, 62248)
12. Quick drying nail polish

Materials-

1. Harvest tumor carefully to ensure structural integrity and place in PFA overnight.
2. Wash tumor tissue with PBS 3X and transfer tissue into a 30% sucrose until the tissue sinks. This step helps to cryoprotect the tissue and prevents ice crystal formation during freezing.

3. Once cryoprotected, flash freeze the tissue in OCT using isopentane and dry ice.
4. The tissue is now ready to be sectioned. The tissue can be stored at -80ºC otherwise.
5. Using cryostat, section tissue into 20 µm thick slices. Plate the sections onto a glass slide.
6. Fix the slides in 4% PFA in PBS for 10 minutes.
7. Rinse slides with PBS 3X.
8. Circles samples with pap pen.
9. Block nonspecific binding by incubating the sections with a blocking solution (1% BSA + 5% goat serum) for 1 hour at room temperature.
10. Incubate with primary antibody diluted in 1% bovine serum albumin (1:100) for 12 hours at 4°C. To stain for vessels, Rabbit anti-mouse CD31 (ab28364, Abcam Inc.) can be used.
11. Rinse slides with PBS 3X.
12. Incubate with secondary antibody diluted in 1% bovine serum albumin (1:250) for 1 hour at room temperature. Goat anti-Rabbit IgG Alexa Fluor™ 647 is used as the secondary antibody.
13. At this point, thaw mountant.
14. Rinse slides with PBS 3X.
15. To stain the cell nucleus, incubate with DAPI diluted in PBS (1:1000) for 10 min.
16. Rinse slides with PBS 3X.
17. Mount with mounting medium and coverslip. Seal sample with quick drying nail polish.

REFERENCES

[1] Y. Okabe and R. Medzhitov, "Tissue biology perspective on macrophages," *Nat Immunol*, vol. 17, no. 1, pp. 9–17, Jan. 2016, doi: 10.1038/ni.3320.

[2] R. Weissleder, M. Nahrendorf, and M. J. Pittet, "Imaging macrophages with nanoparticles," *Nature Materials*, vol. 13, no. 2, Feb. 2014, doi: 10.1038/nmat3780.

[3] S. Bailly, B. Ferrua, M. Fay, and M. A. Gougerot-Pocidalo, "Differential regulation of IL 6, IL 1 A, IL 1β and TNFα production in LPS-stimulated human monocytes: Role of cyclic AMP," *Cytokine*, vol. 2, no. 3, pp. 205–210, May 1990, doi: 10.1016/1043-4666(90)90017-N.

[4] C. Bogdan, J. Paik, Y. Vodovotz, and C. Nathan, "Contrasting mechanisms for suppression of macrophage cytokine release by transforming growth factor-beta and interleukin-10," *Journal of Biological Chemistry*, vol. 267, no. 32, pp. 23301–23308, Nov. 1992, doi: 10.1016/S0021-9258(18)50091-0.

[5] T. A. Wynn and K. M. Vannella, "Macrophages in Tissue Repair, Regeneration, and Fibrosis," *Immunity*, vol. 44, no. 3, pp. 450–462, Mar. 2016, doi: 10.1016/j.immuni.2016.02.015.

[6] M. D. Park, A. Silvin, F. Ginhoux, and M. Merad, "Macrophages in health and disease," *Cell*, vol. 185, no. 23, pp. 4259–4279, Nov. 2022, doi: 10.1016/j.cell.2022.10.007.

[7] C. E. Green *et al.*, "Chemoattractant Signaling between Tumor Cells and Macrophages Regulates Cancer Cell Migration, Metastasis and Neovascularization," *PLoS ONE*, vol. 4, no. 8, p. e6713, Aug. 2009, doi: 10.1371/journal.pone.0006713.

[8] C. Murdoch, A. Giannoudis, and C. E. Lewis, "Mechanisms regulating the recruitment of macrophages into hypoxic areas of tumors and other ischemic tissues," *Blood*, vol. 104, no. 8, pp. 2224–2234, Oct. 2004, doi: 10.1182/blood-2004-03-1109.

[9] P. Kelly, R. Davison, E. Bliss, and J. McGee, "Macrophages in human breast disease: a quantitative immunohistochemical study," *Br J Cancer*, vol. 57, no. 2, pp. 174–177, Feb. 1988, doi: 10.1038/bjc.1988.36.

[10] M. D. Sørensen, R. H. Dahlrot, H. B. Boldt, S. Hansen, and B. W. Kristensen, "Tumour-associated microglia/macrophages predict poor prognosis in high-grade gliomas and correlate with an aggressive tumour subtype," *Neuropathol Appl Neurobiol*, vol. 44, no. 2, pp. 185–206, Feb. 2018, doi: 10.1111/nan.12428.

[11] M. D. Sørensen, R. H. Dahlrot, H. B. Boldt, S. Hansen, and B. W. Kristensen, "Tumour-associated microglia/macrophages predict poor prognosis in high-grade gliomas and correlate with an aggressive tumour subtype," *Neuropathology and Applied Neurobiology*, vol. 44, no. 2, pp. 185–206, 2018, doi: 10.1111/nan.12428.

[12] M. Klichinsky *et al.*, "Human chimeric antigen receptor macrophages for cancer immunotherapy," *Nat Biotechnol*, vol. 38, no. 8, Art. no. 8, Aug. 2020, doi: 10.1038/s41587-020-0462-y.

[13] M. F. Kircher, S. S. Gambhir, and J. Grimm, "Noninvasive cell-tracking methods," *Nat Rev Clin Oncol*, vol. 8, no. 11, pp. 677–688, Nov. 2011, doi: 10.1038/nrclinonc.2011.141.

[14] M. Iafrate and G. O. Fruhwirth, "How Non-invasive in vivo Cell Tracking Supports the Development and Translation of Cancer Immunotherapies," *Frontiers in Physiology*, vol. 11, 2020, Accessed: Feb. 25, 2023. [Online]. Available: https://www.frontiersin.org/articles/10.3389/fphys.2020.00154

[15] I. J. M. de Vries *et al.*, "Magnetic resonance tracking of dendritic cells in melanoma patients for monitoring of cellular therapy," *Nature Biotechnology*, vol. 23, no. 11, Nov. 2005, doi: 10.1038/nbt1154.

[16] E. T. Ahrens and J. Zhong, "*In vivo* MRI cell tracking using perfluorocarbon probes and fluorine-19 detection: *IN VIVO* CELL TRACKING USING ^{19} F MRI," *NMR Biomed.*, vol. 26, no. 7, pp. 860–871, Jul. 2013, doi: 10.1002/nbm.2948.

[17] E. T. Ahrens, B. M. Helfer, C. F. O'Hanlon, and C. Schirda, "Clinical cell therapy imaging using a perfluorocarbon tracer and fluorine-19 MRI," *Magn. Reson. Med.*, vol. 72, no. 6, pp. 1696–1701, Dec. 2014, doi: 10.1002/mrm.25454.

[18] K. O. Jung *et al.*, "Whole-body tracking of single cells via positron emission tomography," *Nat Biomed Eng*, vol. 4, no. 8, pp. 835–844, Jun. 2020, doi: 10.1038/s41551-020-0570-5.

[19] Y. Vedvyas *et al.*, "Longitudinal PET imaging demonstrates biphasic CAR T cell responses in survivors," *JCI Insight*, vol. 1, no. 19, Nov. 2016, doi: 10.1172/jci.insight.90064.

[20] M. A. Sellmyer *et al.*, "Imaging CAR T Cell Trafficking with eDHFR as a PET Reporter Gene," *Molecular Therapy*, vol. 28, no. 1, pp. 42–51, Jan. 2020, doi: 10.1016/j.ymthe.2019.10.007.

[21] J. Kim *et al.*, "Use of Nanoparticle Contrast Agents for Cell Tracking with Computed Tomography," *Bioconjugate Chem.*, vol. 28, no. 6, pp. 1581–1597, Jun. 2017, doi: 10.1021/acs.bioconjchem.7b00194.

[22] A. Seth, H. Park, and K. Hong, “Current Perspective on In Vivo Molecular Imaging of Immune Cells,” *Molecules*, vol. 22, no. 6, pp. 881–881, May 2017, doi: 10.3390/molecules22060881.

[23] J. W. M. Bulte and H. E. Daldrup-Link, “Clinical Tracking of Cell Transfer and Cell Transplantation: Trials and Tribulations,” *Radiology*, vol. 289, no. 3, pp. 604–615, Dec. 2018, doi: 10.1148/radiol.2018180449.

[24] E. T. Ahrens, B. M. Helfer, C. F. O’Hanlon, and C. Schirda, “Clinical cell therapy imaging using a perfluorocarbon tracer and fluorine-19 MRI,” *Magn. Reson. Med.*, vol. 72, no. 6, pp. 1696–1701, Dec. 2014, doi: 10.1002/mrm.25454.

[25] T. Kim *et al.*, “In Vivo Micro-CT Imaging of Human Mesenchymal Stem Cells Labeled with Gold-Poly- L -Lysine Nanocomplexes,” *Adv. Funct. Mater.*, vol. 27, no. 3, p. 1604213, Jan. 2017, doi: 10.1002/adfm.201604213.

[26] C. Zong, A. Bronckaers, G. Vande Velde, G. Willems, and M. Cadenas de Llano-Pérula, “In Vivo Micro-Computerized Tomography Tracking of Human Periodontal Ligament Stem Cells Labeled with Gold Nanocomplexes,” *Adv Healthcare Materials*, vol. 11, no. 1, p. 2101133, Jan. 2022, doi: 10.1002/adhm.202101133.

[27] E. J. Sutton, T. D. Henning, B. J. Pichler, C. Bremer, and H. E. Daldrup-Link, “Cell tracking with optical imaging,” *Eur Radiol*, vol. 18, no. 10, pp. 2021–2032, Oct. 2008, doi: 10.1007/s00330-008-0984-z.

[28] G. H. Simon *et al.*, “Optical imaging of experimental arthritis using allogeneic leukocytes labeled with a near-infrared fluorescent probe,” *Eur J Nucl Med Mol Imaging*, vol. 33, no. 9, pp. 998–1006, Aug. 2006, doi: 10.1007/s00259-006-0081-y.

[29] E. Chorniak *et al.*, “Intravital optical imaging for immune cell tracking after photoimmunotherapy with plasmonic gold nanostars,” *Nanotechnology*, vol. 33, no. 47, p. 475101, Nov. 2022, doi: 10.1088/1361-6528/ac893a.

[30] J. Comenge *et al.*, “Preventing Plasmon Coupling between Gold Nanorods Improves the Sensitivity of Photoacoustic Detection of Labeled Stem Cells *in Vivo*,” *ACS Nano*, vol. 10, no. 7, pp. 7106–7116, Jul. 2016, doi: 10.1021/acsnano.6b03246.

[31] E. M. Donnelly, K. P. Kubelick, D. S. Dumani, and S. Y. Emelianov, “Photoacoustic Image-Guided Delivery of Plasmonic-Nanoparticle-Labeled Mesenchymal Stem Cells to the Spinal Cord,” *Nano Lett.*, vol. 18, no. 10, pp. 6625–6632, Oct. 2018, doi: 10.1021/acs.nanolett.8b03305.

[32] W. Cui *et al.*, “Neural progenitor cells labeling with microbubble contrast agent for ultrasound imaging in vivo,” *Biomaterials*, vol. 34, no. 21, pp. 4926–4935, Jul. 2013, doi: 10.1016/j.biomaterials.2013.03.020.

[33] J. Mamou and M. L. Oelze, Eds., *Quantitative Ultrasound in Soft Tissues*. Dordrecht: Springer Netherlands, 2013. doi: 10.1007/978-94-007-6952-6.

[34] P. M. Morse and K. U. Ingard, *Theoretical acoustics*. Princeton, N.J: Princeton University Press, 1986.

[35] J. W. Strutt, "XV. *On the light from the sky, its polarization and colour*," *The London, Edinburgh, and Dublin Philosophical Magazine and Journal of Science*, vol. 41, no. 271, pp. 107–120, Feb. 1871, doi: 10.1080/14786447108640452.

[36] X. Cao, S. Maharjan, R. Ashfaq, J. Shin, and Y. S. Zhang, "Bioprinting of Small-Diameter Blood Vessels," *Engineering*, vol. 7, no. 6, pp. 832–844, Jun. 2021, doi: 10.1016/j.eng.2020.03.019.

[37] N. de Jong, "Acoustic properties of ultrasound contrast agents," Ph.D. thesis, Erasmus University Rotterdam, 1993. [Online]. Available: http://hdl.handle.net/1765/39138

[38] P. A. Dayton and K. W. Ferrara, "Targeted imaging using ultrasound," *J. Magn. Reson. Imaging*, vol. 16, no. 4, pp. 362–377, Oct. 2002, doi: 10.1002/jmri.10173.

[39] A. L. Anderson and L. D. Hampton, "Acoustics of gas-bearing sediments I. Background," *The Journal of the Acoustical Society of America*, vol. 67, no. 6, pp. 1865–1889, Jun. 1980, doi: 10.1121/1.384453.

[40] S. Sirsi, J. Feshitan, J. Kwan, S. Homma, and M. Borden, "Effect of Microbubble Size on Fundamental Mode High Frequency Ultrasound Imaging in Mice," *Ultrasound in Medicine & Biology*, vol. 36, no. 6, pp. 935–948, Jun. 2010, doi: 10.1016/j.ultrasmedbio.2010.03.015.

[41] A. BØyum, H. Brincker Fjerdingstad, I. Martinsen, T. Lea, and D. LØvhaug, "Separation of Human Lymphocytes from Citrated Blood by Density Gradient (NycoPrep) Centrifugation: Monocyte Depletion Depending upon Activation of Membrane Potassium Channels: Separation of Lymphocytes," *Scandinavian Journal of Immunology*, vol. 56, no. 1, pp. 76–84, Jul. 2002, doi: 10.1046/j.1365-3083.2002.01102.x.

[42] Q. Fu, Y. Zhang, T. Huang, and Y. Liu, "Measurement of the Compressibility of Cell and Nucleus Based on Acoustofluidic Microdevice," *JoVE*, no. 185, p. 64225, Jul. 2022, doi: 10.3791/64225.

[43] D. Hartono, Y. Liu, P. L. Tan, X. Y. S. Then, L.-Y. L. Yung, and K.-M. Lim, "On-chip measurements of cell compressibility via acoustic radiation," *Lab Chip*, vol. 11, no. 23, p. 4072, 2011, doi: 10.1039/c1lc20687g.

[44] D. E. Goertz, N. De Jong, and A. F. W. Van Der Steen, "Attenuation and Size Distribution Measurements of Definity™ and Manipulated Definity™ Populations,"

Ultrasound in Medicine & Biology, vol. 33, no. 9, pp. 1376–1388, Sep. 2007, doi: 10.1016/j.ultrasmedbio.2007.03.009.

[45] T. Faez, D. Goertz, and N. De Jong, "Characterization of Definity™ Ultrasound Contrast Agent at Frequency Range of 5–15 MHz," *Ultrasound in Medicine & Biology*, vol. 37, no. 2, pp. 338–342, Feb. 2011, doi: 10.1016/j.ultrasmedbio.2010.11.014.

[46] A. J. Sojahrood, H. Haghi, Q. Li, T. M. Porter, R. Karshafian, and M. C. Kolios, "Nonlinear power loss in the oscillations of coated and uncoated bubbles: Role of thermal, radiation and encapsulating shell damping at various excitation pressures," *Ultrasonics Sonochemistry*, vol. 66, p. 105070, Sep. 2020, doi: 10.1016/j.ultsonch.2020.105070.

[47] P. R. Hoskins, K. Martin, and A. Thrush, Eds., *Diagnostic Ultrasound: Physics and Equipment*, 2nd ed. Cambridge University Press, 2010. doi: 10.1017/CBO9780511750885.

[48] Z. Xu, H. Liu, H. Tian, and F. Yan, "Real-Time Imaging Tracking of Engineered Macrophages as Ultrasound-Triggered Cell Bombs for Cancer Treatment," *Advanced Functional Materials*, vol. 30, no. 14, pp. 1910304–1910304, Apr. 2020, doi: 10.1002/adfm.201910304.

[49] J. R. Lindner *et al.*, "Noninvasive Imaging of Inflammation by Ultrasound Detection of Phagocytosed Microbubbles," *Circulation*, vol. 102, no. 5, pp. 531–538, Aug. 2000, doi: 10.1161/01.CIR.102.5.531.

[50] M. Ahmed *et al.*, "Cellular Uptake of Plain and SPION-Modified Microbubbles for Potential Use in Molecular Imaging," *Cellular and Molecular Bioengineering*, vol. 10, no. 6, pp. 537–548, Dec. 2017, doi: 10.1007/s12195-017-0504-9.

[51] D. Paul, S. Achouri, Y.-Z. Yoon, J. Herre, C. E. Bryant, and P. Cicuta, "Phagocytosis Dynamics Depends on Target Shape," *Biophysical Journal*, vol. 105, no. 5, pp. 1143–1150, Sep. 2013, doi: 10.1016/j.bpj.2013.07.036.

[52] H. Suganuma, J. W. Fahey, K. E. Bryan, Z. R. Healy, and P. Talalay, "Stimulation of phagocytosis by sulforaphane," *Biochemical and Biophysical Research Communications*, vol. 405, no. 1, pp. 146–151, Feb. 2011, doi: 10.1016/j.bbrc.2011.01.025.

[53] R. Weissleder, M. Nahrendorf, and M. J. Pittet, "Imaging macrophages with nanoparticles," *Nature Materials*, vol. 13, no. 2, Feb. 2014, doi: 10.1038/nmat3780.

[54] R. Zhao *et al.*, "Phosphatidylserine-microbubble targeting-activated microglia/macrophage in inflammation combined with ultrasound for breaking through the blood–brain barrier," *J Neuroinflammation*, vol. 15, no. 1, p. 334, Dec. 2018, doi: 10.1186/s12974-018-1368-1.

[55] K. Yanagisawa, F. Moriyasu, T. Miyahara, M. Yuki, and H. Iijima, “Phagocytosis of ultrasound contrast agent microbubbles by Kupffer cells,” *Ultrasound in Medicine & Biology*, vol. 33, no. 2, pp. 318–325, Feb. 2007, doi: 10.1016/j.ultrasmedbio.2006.08.008.

[56] R. Bam *et al.*, “Efficacy of Affibody-Based Ultrasound Molecular Imaging of Vascular B7-H3 for Breast Cancer Detection,” *Clinical Cancer Research*, vol. 26, no. 9, pp. 2140–2150, May 2020, doi: 10.1158/1078-0432.CCR-19-1655.

[57] M. R. Böhmer, C. H. T. Chlon, B. I. Raju, C. T. Chin, T. Shevchenko, and A. L. Klibanov, “Focused ultrasound and microbubbles for enhanced extravasation,” *Journal of Controlled Release*, vol. 148, no. 1, pp. 18–24, Nov. 2010, doi: 10.1016/j.jconrel.2010.06.012.

[58] B. Taciak *et al.*, “Evaluation of phenotypic and functional stability of RAW 264.7 cell line through serial passages,” *PLoS ONE*, vol. 13, no. 6, p. e0198943, Jun. 2018, doi: 10.1371/journal.pone.0198943.

[59] J. A. Champion, A. Walker, and S. Mitragotri, “Role of Particle Size in Phagocytosis of Polymeric Microspheres,” *Pharm Res*, vol. 25, no. 8, pp. 1815–1821, Aug. 2008, doi: 10.1007/s11095-008-9562-y.

[60] S.-K. Wu *et al.*, “Characterization of Different Microbubbles in Assisting Focused Ultrasound-Induced Blood-Brain Barrier Opening,” *Sci Rep*, vol. 7, no. 1, p. 46689, Apr. 2017, doi: 10.1038/srep46689.

[61] J. A. Navarro-Becerra, K.-H. Song, P. Martinez, and M. A. Borden, “Microbubble Size and Dose Effects on Pharmacokinetics,” *ACS Biomater. Sci. Eng.*, vol. 8, no. 4, pp. 1686–1695, Apr. 2022, doi: 10.1021/acsbiomaterials.2c00043.

[62] G. Sahay, D. Y. Alakhova, and A. V. Kabanov, “Endocytosis of nanomedicines,” *Journal of Controlled Release*, vol. 145, no. 3, pp. 182–195, Aug. 2010, doi: 10.1016/j.jconrel.2010.01.036.

[63] H.-S. Jeong *et al.*, “Effect of space length of mannose ligand on uptake of mannosylated liposome in RAW 264.7 cells: *In vitro* and *in vivo* studies: EFFECT OF SPACE LENGTH OF MANNOSE LIGAND ON UPTAKE OF MANNOSYLATED LIPOSOME,” *J. Biomed. Mater. Res.*, p. n/a-n/a, Feb. 2014, doi: 10.1002/jbm.a.35112.

[64] P. S. Epstein and M. S. Plesset, “On the Stability of Gas Bubbles in Liquid-Gas Solutions,” *The Journal of Chemical Physics*, vol. 18, no. 11, pp. 1505–1509, Nov. 1950, doi: 10.1063/1.1747520.

[65] C. E. Brennen, *Fundamentals of multiphase flow*. Cambridge [England] ; New York: Cambridge University Press, 2005.

[66] J. E. Chomas, P. Dayton, J. Allen, K. Morgan, and K. W. Ferrara, “Mechanisms of contrast agent destruction,” *IEEE Trans. Ultrason., Ferroelect., Freq. Contr.*, vol. 48, no. 1, pp. 232–248, Jan. 2001, doi: 10.1109/58.896136.

[67] B. D. Lindsey *et al.*, “High Resolution Ultrasound Superharmonic Perfusion Imaging: In Vivo Feasibility and Quantification of Dynamic Contrast-Enhanced Acoustic Angiography,” *Ann Biomed Eng*, vol. 45, no. 4, pp. 939–948, Apr. 2017, doi: 10.1007/s10439-016-1753-9.

[68] S. E. Shelton, B. D. Lindsey, J. K. Tsuruta, F. S. Foster, and P. A. Dayton, “Molecular Acoustic Angiography: A New Technique for High-resolution Superharmonic Ultrasound Molecular Imaging,” *Ultrasound in Medicine & Biology*, vol. 42, no. 3, pp. 769–781, Mar. 2016, doi: 10.1016/j.ultrasmedbio.2015.10.015.

[69] T. Sen, O. Tufekcioglu, and Y. Koza, “Mechanical index,” *Anatol J Cardiol*, vol. 15, no. 4, pp. 334–336, Apr. 2015, doi: 10.5152/akd.2015.6061.

[70] “American Institute of Ultrasound in Medicine Consensus Report on Potential Bioeffects of Diagnostic Ultrasound: Executive Summary,” *Journal of Ultrasound in Medicine*, vol. 27, no. 4, pp. 503–515, Apr. 2008, doi: 10.7863/jum.2008.27.4.503.

[71] R. E. Apfel and C. K. Holland, “Gauging the likelihood of cavitation from short-pulse, low-duty cycle diagnostic ultrasound,” *Ultrasound in Medicine & Biology*, vol. 17, no. 2, pp. 179–185, Jan. 1991, doi: 10.1016/0301-5629(91)90125-G.

[72] S. Chen, E. C. So, S. E. Strome, and X. Zhang, “Impact of Detachment Methods on M2 Macrophage Phenotype and Function,” *Journal of Immunological Methods*, vol. 426, pp. 56–61, Nov. 2015, doi: 10.1016/j.jim.2015.08.001.

[73] L. E. Hind, M. Dembo, and D. A. Hammer, “Macrophage motility is driven by frontal-towing with a force magnitude dependent on substrate stiffness,” *Integr. Biol.*, vol. 7, no. 4, pp. 447–453, 2015, doi: 10.1039/C4IB00260A.

[74] J. W. Pollard, “Trophic macrophages in development and disease,” *Nat Rev Immunol*, vol. 9, no. 4, pp. 259–270, Apr. 2009, doi: 10.1038/nri2528.

[75] C. Shi and E. G. Pamer, “Monocyte recruitment during infection and inflammation,” *Nat Rev Immunol*, vol. 11, no. 11, pp. 762–774, Nov. 2011, doi: 10.1038/nri3070.

[76] S. Boyden, “THE CHEMOTACTIC EFFECT OF MIXTURES OF ANTIBODY AND ANTIGEN ON POLYMORPHONUCLEAR LEUCOCYTES,” *Journal of Experimental Medicine*, vol. 115, no. 3, pp. 453–466, Mar. 1962, doi: 10.1084/jem.115.3.453.

[77] Z. Xu, H. Liu, H. Tian, and F. Yan, “Real-Time Imaging Tracking of Engineered Macrophages as Ultrasound-Triggered Cell Bombs for Cancer Treatment,”

Advanced Functional Materials, vol. 30, no. 14, p. 1910304, 2020, doi: 10.1002/adfm.201910304.

[78] H. Zhang, X. Zhang, Y. Ren, F. Cao, L. Hou, and Z. Zhang, "An in situ microenvironmental nano-regulator to inhibit the proliferation and metastasis of 4T1 tumor," *Theranostics*, vol. 9, no. 12, pp. 3580–3594, 2019, doi: 10.7150/thno.33141.

[79] B. P. Joshi, J. Hardie, M. A. Mingroni, and M. E. Farkas, "Surface-Modified Macrophages Facilitate Tracking of Breast Cancer-Immune Interactions," *ACS Chem. Biol.*, vol. 13, no. 8, pp. 2339–2346, Aug. 2018, doi: 10.1021/acschembio.8b00509.

[80] M. Emmer, H. Vos, M. Versluis, and N. Jong, "Radial modulation of single microbubbles," *IEEE Trans. Ultrason., Ferroelect., Freq. Contr.*, vol. 56, no. 11, pp. 2370–2379, Nov. 2009, doi: 10.1109/TUFFC.2009.1325.

[81] P. N. Burns, D. Hope Simpson, and M. A. Averkiou, "Nonlinear imaging," *Ultrasound in Medicine & Biology*, vol. 26, pp. S19–S22, May 2000, doi: 10.1016/S0301-5629(00)00155-1.

[82] P. N. Burns, "Harmonic imaging: principles and preliminary results," *Clin Radiol*, vol. 51, pp. 50–55, 1996.

[83] K. E. Morgan, J. S. Allen, P. A. Dayton, J. E. Chomas, A. L. Klibaov, and K. W. Ferrara, "Experimental and theoretical evaluation of microbubble behavior: effect of transmitted phase and bubble size," *IEEE Trans. Ultrason., Ferroelect., Freq. Contr.*, vol. 47, no. 6, pp. 1494–1509, Nov. 2000, doi: 10.1109/58.883539.

[84] T. A. Whittingham, "Medical diagnostic applications and sources," *Progress in Biophysics and Molecular Biology*, vol. 93, no. 1–3, pp. 84–110, Jan. 2007, doi: 10.1016/j.pbiomolbio.2006.07.004.

[85] Peng Jiang, Zuhua Mao, and J. C. Lazenby, "A new tissue harmonic imaging scheme with better fundamental frequency cancellation and higher signal-to-noise ratio," in *1998 IEEE Ultrasonics Symposium. Proceedings (Cat. No. 98CH36102)*, Sendai, Japan: IEEE, 1998, pp. 1589–1594. doi: 10.1109/ULTSYM.1998.765248.

[86] C.-C. Shen, Y.-H. Chou, and P.-C. Li, "Pulse Inversion Techniques in Ultrasonic Nonlinear Imaging," *Journal of Medical Ultrasound*, vol. 13, no. 1, pp. 3–17, 2005, doi: 10.1016/S0929-6441(09)60073-4.

[87] M. A. Averkiou, M. F. Bruce, J. E. Powers, P. S. Sheeran, and P. N. Burns, "Imaging Methods for Ultrasound Contrast Agents," *Ultrasound in Medicine & Biology*, vol. 46, no. 3, pp. 498–517, Mar. 2020, doi: 10.1016/j.ultrasmedbio.2019.11.004.

[88] K. G. Brown and K. Hoyt, "Evaluation of Nonlinear Contrast Pulse Sequencing for Use in Super-Resolution Ultrasound Imaging," *IEEE Trans. Ultrason., Ferroelect.,*

Freq. Contr., vol. 68, no. 11, pp. 3347–3361, Nov. 2021, doi: 10.1109/TUFFC.2021.3092172.

[89] B. Jing, E. P. Kashyap, and B. D. Lindsey, "Transcranial activation and imaging of low boiling point phase-change contrast agents through the temporal bone using an ultrafast interframe activation ultrasound sequence," *Med. Phys.*, vol. 47, no. 9, pp. 4450–4464, Sep. 2020, doi: 10.1002/mp.14390.

[90] S. Upadhaya, J. X. Yu, M. Shah, D. Correa, T. Partridge, and J. Campbell, "The clinical pipeline for cancer cell therapies," *Nature Reviews Drug Discovery*, vol. 20, no. 7, pp. 503–504, Jul. 2021, doi: 10.1038/d41573-021-00100-z.

[91] A. R. Saez-Ibañez, S. Upadhaya, T. Partridge, M. Shah, D. Correa, and J. Campbell, "Landscape of cancer cell therapies: trends and real-world data," *Nat Rev Drug Discov*, vol. 21, no. 9, pp. 631–632, Sep. 2022, doi: 10.1038/d41573-022-00095-1.

[92] J. Theruvath *et al.*, "Locoregionally administered B7-H3-targeted CAR T cells for treatment of atypical teratoid/rhabdoid tumors," *Nat Med*, vol. 26, no. 5, pp. 712–719, May 2020, doi: 10.1038/s41591-020-0821-8.

[93] M. Mulazzani *et al.*, "Long-term in vivo microscopy of CAR T cell dynamics during eradication of CNS lymphoma in mice," *Proc. Natl. Acad. Sci. U.S.A.*, vol. 116, no. 48, pp. 24275–24284, Nov. 2019, doi: 10.1073/pnas.1903854116.

[94] P. Sridhar and F. Petrocca, "Regional Delivery of Chimeric Antigen Receptor (CAR) T-Cells for Cancer Therapy," *Cancers*, vol. 9, no. 7, p. 92, Jul. 2017, doi: 10.3390/cancers9070092.

[95] J. Tchou *et al.*, "Safety and Efficacy of Intratumoral Injections of Chimeric Antigen Receptor (CAR) T Cells in Metastatic Breast Cancer," *Cancer Immunology Research*, vol. 5, no. 12, pp. 1152–1161, Dec. 2017, doi: 10.1158/2326-6066.CIR-17-0189.

[96] G. Agliardi *et al.*, "Intratumoral IL-12 delivery empowers CAR-T cell immunotherapy in a pre-clinical model of glioblastoma," *Nat Commun*, vol. 12, no. 1, p. 444, Jan. 2021, doi: 10.1038/s41467-020-20599-x.

[97] P. S. Adusumilli *et al.*, "Regional delivery of mesothelin-targeted CAR T cell therapy generates potent and long-lasting CD4-dependent tumor immunity," *Sci. Transl. Med.*, vol. 6, no. 261, Nov. 2014, doi: 10.1126/scitranslmed.3010162.

[98] L. Weiss, A. Abdul-Hai, R. Or, G. Amir, and A. Polliack, "Fludarabine in combination with cyclophosphamide decreases incidence of GVHD and maintains effective graft-versus-leukemia effect after allogeneic stem cell transplantation in murine lymphocytic leukemia," *Bone Marrow Transplant*, vol. 31, no. 1, pp. 11–15, Jan. 2003, doi: 10.1038/sj.bmt.1703775.

[99] I. Sagiv-Barfi, D. K. Czerwinski, T. Shree, J. J. K. Lohmeyer, and R. Levy, "Intratumoral immunotherapy relies on B and T cell collaboration," *Sci. Immunol.*, vol. 7, no. 71, p. eabn5859, May 2022, doi: 10.1126/sciimmunol.abn5859.

[100] Nina M. Muñoz *et al.*, "Influence of injection technique, drug formulation and tumor microenvironment on intratumoral immunotherapy delivery and efficacy," *J Immunother Cancer*, vol. 9, no. 2, p. e001800, Feb. 2021, doi: 10.1136/jitc-2020-001800.

[101] K. A. Præstmark, B. Stallknecht, M. L. Jensen, T. Sparre, N. B. Madsen, and J. Kildegaard, "Injection Technique and Pen Needle Design Affect Leakage From Skin After Subcutaneous Injections," *J Diabetes Sci Technol*, vol. 10, no. 4, pp. 914–922, Jul. 2016, doi: 10.1177/1932296815626723.

[102] C.-H. Heldin, K. Rubin, K. Pietras, and A. Östman, "High interstitial fluid pressure — an obstacle in cancer therapy," *Nat Rev Cancer*, vol. 4, no. 10, pp. 806–813, Oct. 2004, doi: 10.1038/nrc1456.

[103] C. Sloas, S. Gill, and M. Klichinsky, "Engineered CAR-Macrophages as Adoptive Immunotherapies for Solid Tumors," *Front. Immunol.*, vol. 12, p. 783305, Nov. 2021, doi: 10.3389/fimmu.2021.783305.

[104] M. Martinez and E. K. Moon, "CAR T Cells for Solid Tumors: New Strategies for Finding, Infiltrating, and Surviving in the Tumor Microenvironment," *Front. Immunol.*, vol. 10, p. 128, Feb. 2019, doi: 10.3389/fimmu.2019.00128.

[105] A. Marabelle, L. Tselikas, T. De Baere, and R. Houot, "Intratumoral immunotherapy: using the tumor as the remedy," *Annals of Oncology*, vol. 28, pp. xii33–xii43, Dec. 2017, doi: 10.1093/annonc/mdx683.

[106] F. Combes, S. Mc Cafferty, E. Meyer, and N. N. Sanders, "Off-Target and Tumor-Specific Accumulation of Monocytes, Macrophages and Myeloid-Derived Suppressor Cells after Systemic Injection," *Neoplasia*, vol. 20, no. 8, pp. 848–856, Aug. 2018, doi: 10.1016/j.neo.2018.06.005.

[107] S. R. Sirsi and M. A. Borden, "Microbubble compositions, properties and biomedical applications," *Bubble Science, Engineering & Technology*, vol. 1, no. 1–2, pp. 3–17, Nov. 2009, doi: 10.1179/175889709X446507.

[108] R. Weissleder, M. Nahrendorf, and M. J. Pittet, "Imaging macrophages with nanoparticles," *Nat Mater*, vol. 13, no. 2, pp. 125–138, Feb. 2014, doi: 10.1038/nmat3780.

[109] L. J. Berghaus *et al.*, "Innate immune responses of primary murine macrophage-lineage cells and RAW 264.7 cells to ligands of Toll-like receptors 2, 3, and 4," *Comparative Immunology, Microbiology and Infectious Diseases*, vol. 33, no. 5, pp. 443–454, Sep. 2010, doi: 10.1016/j.cimid.2009.07.001.

[110] M. Kalos and C. H. June, “Adoptive T Cell Transfer for Cancer Immunotherapy in the Era of Synthetic Biology,” *Immunity*, vol. 39, no. 1, pp. 49–60, Jul. 2013, doi: 10.1016/j.immuni.2013.07.002.

[111] D. M. Mosser and J. P. Edwards, “Exploring the full spectrum of macrophage activation,” *Nat Rev Immunol*, vol. 8, no. 12, pp. 958–969, Dec. 2008, doi: 10.1038/nri2448.

[112] G. Arango Duque and A. Descoteaux, “Macrophage Cytokines: Involvement in Immunity and Infectious Diseases,” *Front. Immunol.*, vol. 5, Oct. 2014, doi: 10.3389/fimmu.2014.00491.

[113] A. C. Li and C. K. Glass, “The macrophage foam cell as a target for therapeutic intervention,” *Nature Medicine*, vol. 8, no. 11, pp. 1235–1242, Nov. 2002, doi: 10.1038/nm1102-1235.

[114] C. Yunna, H. Mengru, W. Lei, and C. Weidong, “Macrophage M1/M2 polarization,” *European Journal of Pharmacology*, vol. 877, p. 173090, Jun. 2020, doi: 10.1016/j.ejphar.2020.173090.

[115] A. Mantovani, S. Sozzani, M. Locati, P. Allavena, and A. Sica, “Macrophage polarization: tumor-associated macrophages as a paradigm for polarized M2 mononuclear phagocytes,” *Trends in Immunology*, vol. 23, no. 11, pp. 549–555, Nov. 2002, doi: 10.1016/S1471-4906(02)02302-5.

[116] K. S. Siveen and G. Kuttan, “Role of macrophages in tumour progression,” *Immunology Letters*, vol. 123, no. 2, pp. 97–102, Apr. 2009, doi: 10.1016/j.imlet.2009.02.011.

[117] H. Takiguchi *et al.*, “Macrophages with reduced expressions of classical M1 and M2 surface markers in human bronchoalveolar lavage fluid exhibit pro-inflammatory gene signatures,” *Sci Rep*, vol. 11, no. 1, p. 8282, Apr. 2021, doi: 10.1038/s41598-021-87720-y.

[118] K. Pantel, R. J. Cote, and O. Fodstad, “Detection and Clinical Importance of Micrometastatic Disease,” *JNCI Journal of the National Cancer Institute*, vol. 91, no. 13, pp. 1113–1124, Jul. 1999, doi: 10.1093/jnci/91.13.1113.

[119] A. Aalipour *et al.*, “Engineered immune cells as highly sensitive cancer diagnostics,” *Nat Biotechnol*, vol. 37, no. 5, pp. 531–539, May 2019, doi: 10.1038/s41587-019-0064-8.

[120] Y. M. Sigal, R. Zhou, and X. Zhuang, “Visualizing and discovering cellular structures with super-resolution microscopy,” *Science*, vol. 361, no. 6405, pp. 880–887, Aug. 2018, doi: 10.1126/science.aau1044.

[121] C. Errico *et al.*, “Ultrafast ultrasound localization microscopy for deep super-resolution vascular imaging,” *Nature*, vol. 527, no. 7579, Nov. 2015, doi: 10.1038/nature16066.

[122] F. Lin, S. E. Shelton, D. Espíndola, J. D. Rojas, G. Pinton, and P. A. Dayton, “3-D Ultrasound Localization Microscopy for Identifying Microvascular Morphology Features of Tumor Angiogenesis at a Resolution Beyond the Diffraction Limit of Conventional Ultrasound,” *Theranostics*, vol. 7, no. 1, 2017, doi: 10.7150/thno.16899.

[123] T. Opacic *et al.*, “Motion model ultrasound localization microscopy for preclinical and clinical multiparametric tumor characterization,” *Nature Communications*, vol. 9, no. 1, Dec. 2018, doi: 10.1038/s41467-018-03973-8.

[124] J. Foiret, H. Zhang, T. Ilovitsh, L. Mahakian, S. Tam, and K. W. Ferrara, “Ultrasound localization microscopy to image and assess microvasculature in a rat kidney,” *Scientific Reports*, vol. 7, no. 1, Dec. 2017, doi: 10.1038/s41598-017-13676-7.

[125] O. Couture, V. Hingot, B. Heiles, P. Muleki-Seya, and M. Tanter, “Ultrasound Localization Microscopy and Super-Resolution: A State of the Art,” *IEEE Transactions on Ultrasonics, Ferroelectrics, and Frequency Control*, vol. 65, no. 8, Aug. 2018, doi: 10.1109/TUFFC.2018.2850811.

[126] Y. Desailly, J. Pierre, O. Couture, and M. Tanter, “Resolution limits of ultrafast ultrasound localization microscopy,” *Physics in Medicine and Biology*, vol. 60, no. 22, Nov. 2015, doi: 10.1088/0031-9155/60/22/8723.

[127] K. Christensen-Jeffries *et al.*, “Super-resolution Ultrasound Imaging,” *Ultrasound in Medicine & Biology*, vol. 46, no. 4, Apr. 2020, doi: 10.1016/j.ultrasmedbio.2019.11.013.

[128] S. Schoen, Z. Zhao, A. Alva, C. Huang, S. Chen, and C. Arvanitis, “Morphological Reconstruction Improves Microvessel Mapping in Super-Resolution Ultrasound,” *IEEE Trans. Ultrason., Ferroelect., Freq. Contr.*, vol. 68, no. 6, pp. 2141–2149, Jun. 2021, doi: 10.1109/TUFFC.2021.3057540.

[129] J. Nagy, S.-H. Chang, S.-C. Shih, A. Dvorak, and H. Dvorak, “Heterogeneity of the Tumor Vasculature,” *Semin Thromb Hemost*, vol. 36, no. 03, pp. 321–331, Apr. 2010, doi: 10.1055/s-0030-1253454.

[130] E. Van Goethem, R. Poincloux, F. Gauffre, I. Maridonneau-Parini, and V. Le Cabec, “Matrix Architecture Dictates Three-Dimensional Migration Modes of Human Macrophages: Differential Involvement of Proteases and Podosome-Like Structures,” *The Journal of Immunology*, vol. 184, no. 2, pp. 1049–1061, Jan. 2010, doi: 10.4049/jimmunol.0902223.